

A pressure-based force and torque prediction technique for the study of fish-like swimming

Kelsey N. Lucas^{1,*}, John O. Dabiri², and George V. Lauder¹

¹ Museum of Comparative Zoology, Harvard University, Cambridge, MA 02138, USA

² Departments of Civil & Environmental Engineering and Mechanical Engineering, Stanford University, Stanford, CA 94305, USA

*Corresponding author

E-mail: kelsey.n.lucas@gmail.com

Short title: Pressure-based calculation of swimming forces and torques

1 **Abstract**

2 Many outstanding questions about the evolution and function of fish morphology are
3 linked to swimming dynamics, and a detailed knowledge of time-varying forces and torques
4 along the animal’s body is a key component in answering many of these questions. Yet,
5 quantifying these forces and torques experimentally represents a major challenge that to date
6 prevents a full understanding of fish-like swimming. Here, we develop a method for obtaining
7 these force and torque data non-invasively using standard 2D digital particle image velocimetry
8 in conjunction with a pressure field algorithm. We use a mechanical flapping foil apparatus to
9 model fish-like swimming and measure forces and torques directly with a load cell, and compare
10 these measured values to those estimated simultaneously using our pressure-based approach. We
11 demonstrate that, when out-of-plane flows are relatively small compared to the planar flow, and
12 when pressure effects sufficiently dominate shear effects, this technique is able to accurately
13 reproduce the shape, magnitude, and timing of locomotor forces and torques experienced by a
14 fish-like swimmer. We conclude by exploring of the limits of this approach and its feasibility in
15 the study of freely-swimming fishes.

16

17

18 **Introduction**

19 Fishes display a remarkable array of morphologies, which they use to play many different
20 types of ecological roles, from grazers to apex predators. This diversity in form and function has
21 arisen from many selective pressures, and a number of these pressures are related to locomotion
22 [1–4]. Fish need to evade predators, capture prey, migrate, and move through complex
23 environments. As such, many outstanding questions about the relationships between form and
24 function in fish are biomechanically-driven. For example, understanding how body shape
25 influences swimming specializations [5,6], how material properties of the body dictate
26 swimming performance [7–11], and the relative contributions of individual fins to overall
27 movement [12,13] all remain largely unresolved issues in the study of aquatic locomotion.
28 While many approaches, including computational (e.g., [9,13]), physical modeling (e.g.,
29 [7,11,14,15]), and experimental (e.g., [12,16,17]), can be taken to answer these questions, one
30 promising approach is to leverage a detailed understanding of the magnitudes and distributions
31 of the time-varying forces and torques that fishes generate to effect locomotion [18–21]. Despite
32 the value of this information for understanding biological swimming, fish evolution, and
33 developing bioinspired underwater vehicles, the nature of a fish’s fluid environment renders
34 direct measurements of forces and torques impractical.

35 Herein, we propose a technique for estimating the forces and torques acting on the body
36 of a fish-like swimmer using an indirect pressure-based approach. Because of the difficulty in
37 measuring locomotor forces and torques directly, we instead obtain the desired force and torque
38 information through knowledge of the surrounding fluid dynamics, following in the tradition of
39 existing strategies such as those proposed by Noca et al. [22], Dabiri [20], and van Oudheusden
40 et al. [23]. The force of the fluid acting on the animal’s body can be given as Eq. 1: the sum of

41 pressure and shear (viscous) forces acting at the animal's surface [24–26].

$$42 \quad \mathbf{F}(t) = - \int \mathbf{n} p \, dA + \int \boldsymbol{\tau} \cdot \mathbf{n} \, dA \quad (1)$$

43 The corresponding torque is given by:

$$44 \quad \mathbf{T}(t) = - \int p (\mathbf{r} \times \mathbf{n}) \, dA + \int \mathbf{r} \times (\boldsymbol{\tau} \cdot \mathbf{n}) \, dA \quad (2)$$

45 Bold indicates vector or tensor quantities: \mathbf{n} is the normal unit vector indicating the direction
46 perpendicularly outward from the body, $\boldsymbol{\tau}$ is the viscous stress tensor, \mathbf{F} is the force acting on the
47 body, \mathbf{T} is the torque acting on the body, and \mathbf{r} is the moment arm vector, measured from the
48 center of rotation (center of mass, for a fish). Additionally, t is time, A describes surface area,
49 and p is pressure in the fluid.

50 The simplicity of these equations has a useful consequence: when the shear forces and
51 torques are small, total forces and torques can be estimated from the pressure terms alone. At the
52 relatively high Reynolds numbers (Re) where many fishes operate (10,000-5,000,000 [24,25]),
53 the shear contributions are small enough that we can still arrive at an accurate estimate of forces
54 and torques using the pressure terms while ignoring the shear terms. Formally, Bale et al. [27]
55 demonstrated this approximation to be reasonable for a fish-like swimmer in their decomposition
56 of locomotor forces into components derived from viscous- and pressure-based effects.

57 Forces and torques could be easily approximated from pressures via Eq. 1 and 2 if
58 pressure could be readily measured, but directly obtaining pressure measurements around a
59 freely-moving body has also proven to be difficult. Pressure sensors can be challenging to apply
60 and may involve animal surgery [28,29]. Additionally, large numbers of sensors are required to
61 provide detailed flow information over the whole body [23,28–31]. More problematically,
62 sensors and their attached cables may interfere with the fluid flow around the animal and
63 therefore will provide, at best, approximations of the pressures around a body that occur during

64 non-invasive study [30,32]. Recently, several methods for calculating pressure fields have been
65 proposed (e.g., [23,30,33–35]). These methods rely on experimentally-measured velocity data
66 and on the Navier-Stokes equations describing fluid motion. The equations are used to calculate
67 pressure by integrating the pressure gradient term along paths through the velocity field (e.g.,
68 [30,33]). Note that the simplification of Eq. 1 and 2 does not imply neglect of viscosity during
69 these pressure field calculations.

70 Measuring flow velocity around biological swimmers is commonly accomplished using
71 two-dimensional digital particle image velocimetry (DPIV) (e.g., [36–38]), by tracking the
72 motions of near-neutrally-buoyant particles in a plane illuminated by a laser light sheet [39,40].
73 The advantages of the 2D approach include the ease with which the position of the animal can be
74 tracked and the flow patterns can be visualized and interpreted, as well as the limited effects on
75 animal behavior and relative ease in convincing the animals to swim with their whole bodies in a
76 light sheet [36–38,40]. While taking a 2D approach to measuring velocity is highly desirable, it
77 also introduces the assumption inherent to 2D DPIV analysis – that the flow perpendicular to the
78 imaging plane is limited [40].

79 Thus, we focus here on validating this approach, i.e., calculating forces and torques from
80 a thin plane of measured velocity data and the corresponding pressure field. To do this, we used
81 a physical model to produce empirical, biologically-relevant flows. In this system, we can
82 measure forces and torques using a load cell, while simultaneously applying our proposed
83 pressure-based technique to estimate these same forces and torques. We then performed a
84 quantitative comparison of the measured and estimated values to identify the conditions where
85 our assumptions – first, that pressure effects dominate shear effects, and second, that most of the
86 fluid’s velocity is captured in the horizontal imaging plane – are met for fish-like swimmers, and

87 reasonable estimates of forces and torques can be produced.

88 In the second section, we describe the physical model of fish-like swimming and the
89 measurement of forces and torques. We also describe the pressure-based calculations used to
90 estimate these same values. In the third section, we describe and compare the measured and
91 estimated forces and torques. In the final section, we discuss the conditions where the
92 measurements and estimates match, and the utility and limitations of this approach for the study
93 of biological locomotion.

94

95 **Methods**

96 **Simultaneous data collection**

97 **Foil design**

98 The principal foil design was based on the “3_3” rectangular foil from Lucas et al. [11],
99 where three layers of transmatte plastic shim stock (ARTUS Corp, Englewood, NJ, USA) were
100 bonded with transparent epoxy. This created a foil of flexural stiffness $EI=5.5 \times 10^{-5} \text{ Nm}^2$. Two
101 versions of this foil were constructed. In the first (Fig 1A), prior to construction, the transmatte
102 finish was removed from a narrow strip at the foil’s midline, using 90% ethanol, on each of the
103 three layers of plastic, creating a transparent window. After construction, a thin strip of
104 fluorescent paint was added just above this window. In the second version (Fig 1B), all of the
105 transmatte finish was removed from each layer of plastic, and three strips of fluorescent paint
106 were added. All of these modifications facilitated imaging.

107

108 **Fig. 1. Schematics of experimental foils.**

109 (A) Rectangular foil. (B) Rectangular foil for 3D testing. (C) Tail-shaped foil. All dimensions
110 are given in centimeters.
111

112 In addition, one foil of a more complex shape was constructed, based on Feilich and
113 Lauder's [41] Shape 2. This tail-shaped foil featured a narrow caudal peduncle and a triangular
114 tail (Fig 1C). This foil was crafted from 1 mm thick clear plastic shim stock (ARTUS Corp,
115 Englewood, NJ, USA) with a flexural stiffness $EI = 6.91 \times 10^{-5} \text{ Nm}^2$ [15]. Strips of fluorescent
116 paint were applied to this foil at the midline and displaced 2.25 cm downward from the midline,
117 so as to cross the gap between the body and tail regions of the foil (Fig 1C).

118 The flexural stiffnesses of all three foils were within the range values found in fish [7].
119

120 **Flapping-foil system**

121 Foils were actuated into oncoming flows using the mechanical flapping-foil system
122 described by Lucas et al. [11] and depicted in Fig 2A. In brief, the leading edge of the foil was
123 clamped by a rod formed by two aluminum spars with rectangular cross-section, each having a
124 chord length of 10 mm and thickness 1.5 mm. An ATI Nano-17 six-axis force-torque sensor
125 (model SI-50-0.50, ATI Industrial Automation, Apex, NC, USA; resolution: forces = 1/80 N,
126 torques = 1/16 Nm) attached to the rod enabled measurements in the X (streamwise), Y (lateral),
127 and Z (vertical) directions. This assembly was suspended in a recirculating flume by a carriage
128 on top of the tank. A set of heave and pitch motors on this carriage actuated the foil. A suite of
129 custom LabVIEW (National Instruments Corp., Austin, TX, USA) programs were used to
130 control foil motion and collect position and force and torque data. Each experimental trial was
131 conducted twice: once with the foil and the rod, and once with only the rod.

132

133 **Fig. 2. Schematics of testing systems.**

134 (A) Mechanical flapping foil testing apparatus in isometric view. (B) Overhead view of the
135 transverse imaging setup. (C) Overhead view of the light sheet path of Laser 1. (D) Overhead
136 view of the light sheet path of Laser 2. Laser 1 and Laser 2 were used simultaneously.
137

138 **Imaging systems**

139 Flow was rendered visible by seeding the flow tank with near-neutrally-buoyant (density
140 1060 kg/m^3), VESTOSINT 1164 white nylon 12 particles with an average diameter of $50 \mu\text{m}$
141 (Degussa Corporation, Piscataway, NJ, USA; now Evonik Industries AG, Essen, GER). These
142 particles and the foil were illuminated with light sheets generated by a continuous wave laser
143 (either Coherent 10W argon-ion or OptoEngine 532A solid-state lasers).

144 To allow automated kinematics detection during later analyses, the illuminated foils
145 needed to be in high contrast with the dark background. In addition, the force and torque
146 estimation method required pressure information from both sides of the foil. Therefore, the flow
147 visualizations could not have any shadows, i.e., places where flow information would be
148 missing. To this end, a set of three mirrors was used in conjunction with the foils' transparent
149 strips and fluorescent paint (Figs 1 and 2) to reflect the laser light and illuminate each foil and
150 the entirety of the surrounding water. Two small, rectangular mirrors were fitted with adjustable
151 mirror mounts, and each was attached to the end of a shaft. These "shaft mirrors" were
152 suspended from the far side of the flow tank: one upstream of the foil, and one downstream (Figs
153 2C and 2D). These mirrors were positioned at an angle to the wall of the tank so as to each
154 reflect light back toward the foil (Figs 2C and 2D). The final mirror was positioned on a stage
155 between the incoming laser and the flow tank (Fig 2D).

156 The lighting scheme worked as follows. The first laser sheet was aimed at the bottom
157 edge of the foil's fluorescent paint (Fig 2C), causing the foil to be the brightest object in the field

158 of view, in contrast to a black background. This first laser sheet also illuminated the flow
159 upstream of the foil and was reflected off the upstream shaft mirror to eliminate the shadow from
160 the foil's rod (Fig 2C). The second laser sheet was aimed through the window in the foil (Fig
161 2D), about 1 mm below the first sheet. This illuminated the flow on the far side of the foil (Fig
162 2D). This laser sheet also was reflected onto the fluorescent paint at the foil's trailing edge, by
163 both the downstream shaft mirror and the mirror outside the tank (Fig 2D). The reflections from
164 these mirrors aided in illuminating the trailing edge of the foil, which tended to curve so as to
165 create shadows.

166 Because surface waves created glare which distorted images of particle motion and
167 introduced error into foil tracking, a set of baffles lined with black foam were placed at the water
168 surface upstream and downstream of the rod, effectively removing the free surface. The baffles
169 suppressed the surface waves, thereby removing glare and ensuring a uniform, dark background
170 that contrasted with the bright foil.

171 Ventral views of the flow tank were filmed at 1000 frames per second using a high-speed
172 camera (Photron PCI-1024; 1024x1024 resolution, 17 μm pixel size) and a 45° mirror positioned
173 below the tank (Fig 2A). The camera was activated upon receiving a LabVIEW pulse trigger,
174 which allowed these data to be collected simultaneously with position, force, and torque data. In
175 all cases, data were collected for the duration of three complete motion cycles.

176 During investigations of 3D effects, vertical flow magnitudes were also measured. An
177 OptoEngine 532A solid-state laser light sheet was projected vertically to illuminate the foil and
178 surrounding flow in a transverse section (Fig 2B). The laser was positioned so as to intersect
179 each foil 2 cm upstream of its trailing edge. A Photron Fastcam Mini AX50 (1024x1024 pixel
180 resolution, 20 μm pixel size) high speed camera collected video at 1000 frames per second off of

181 a single 45° mirror located downstream of the foil (Fig 2B) for three replicate motion cycles.

182

183 **Types of tests conducted and actuation parameters**

184 Each test that involved motion of a foil was conducted twice, once in each of two motion
185 programs. The first program, a heaving program, actuated the foil in sinusoidal, lateral heaving
186 motions without introducing pitch. This program has been used extensively in previous study of
187 foil locomotion [11,14,42–44]. Moreover, we expected that the relatively large degree of flow
188 separation at the foil’s leading edge induced by this program would reveal the sensitivity of the
189 force estimation method to the presence of complex flow structures around the body.

190 The second program featured 0° angle of attack motion [11]. Here, the pitch angle of the
191 foil’s leading edge was continuously changed as the foil heaved laterally so as to maintain a
192 constant 0° geometric angle of attack into the oncoming flow. Compared to the heaving
193 program, this program has been demonstrated to lead to more fish-like kinematics [11,15] and
194 improved swimming performance, in fact, to near-maximum [11,45]. To account for the rotation
195 of the force-torque sensor’s axes during pitch, the measured force values ($F_{x,meas}$ and $F_{y,meas}$)
196 were resolved into streamwise (F_x) and lateral (F_y) components using Eq. 3 and Eq. 4, where θ
197 was the instantaneous pitch angle in radians [11].

$$198 \quad F_x = F_{x,meas} \cos \theta + F_{y,meas} \sin \theta \quad (3)$$

$$199 \quad F_y = -F_{x,meas} \sin \theta + F_{y,meas} \cos \theta \quad (4)$$

200 In each motion program, several types of tests were conducted so as to explore the limits
201 of pressure-based force and torque estimation. The first of these tests was the dynamic test,
202 which was conducted with the rectangular foil with one paint strip/window (Fig 1A). In these
203 tests, the foil’s leading edge heave amplitude and the flow speed were fixed at 1.5 cm and 30

204 cm/s, respectively, and the flapping frequency was ramped up from 0.5 Hz to 2.5 Hz in 0.5 Hz
205 steps. These frequencies are within the range of those used by the caudal fin of a fish, with the
206 upper limit constrained by the capabilities of the flapping-foil system [16,46,47]. The foils
207 therefore swam in accelerating, decelerating, and steady conditions, at $Re = 54,000$ and in a
208 Strouhal number (St) range 0.06-0.53, where Re was based on foil chord-length, and St was
209 based on peak-to-peak trailing edge amplitude. This test was designed to reveal how sensitive
210 the force calculation was to transient flows when velocity information was gathered at the foil
211 midline, where three-dimensional effects are expected to be minimal.

212 The second test, the 3D test, was conducted using the rectangular foil with three strips of
213 paint (Fig 1B) and the tail-shaped foil (Fig 1C). Here, the heave amplitude, actuation frequency,
214 and the flow speed were all fixed, to 1.5 cm, 1.5 Hz, and 30 cm/s, respectively, leading to an Re
215 range of 54,000-55,500 and St range of 0.15-0.43, where again Re was based on foil chord-
216 length, and St was based on peak-to-peak trailing edge amplitude. Initially, the light sheet was
217 positioned at the midline as in the dynamic tests described above. Then, the light sheet was
218 shifted vertically so as to illuminate, in turn, the each of the other paint strips. We anticipated
219 that these locations would experience different degrees of out-of-plane flow due to increasing
220 edge effects. Moreover, the tail-shaped foil could experience complex, interacting flows
221 between the “body” and “tail” regions. Thus, this test would reveal how sensitive the force
222 calculations were to deviations from 2D flow. In addition, the transverse light sheet imaging
223 scheme was used to quantify how strong the vertical flows were around both foils.

224 The third test, the static test, was conducted with the rectangular foil with one paint
225 strip/window (Fig 1A), 0° pitch, and flow speeds 10, 30, and 50 cm/s ($Re = 18,000, 54,000,$ and
226 $90,000$, respectively). Unlike in the previous tests, a deliberately misaligned force-torque sensor

227 was used, as the near-zero magnitude of the lateral forces expected here would be within the
228 sensor's alignment error (± 0.01 N). By misaligning the sensor, larger "lateral" force magnitudes
229 would be registered (and slightly smaller "streamwise" forces), and these could be resolved back
230 into the true streamwise and lateral forces. This was accomplished using Eq. 3 and Eq. 4, while
231 setting the pitch angle to a constant 0° .

232 For each test, data were collected for three replicate motion cycles. In the static case
233 where no motion cycle was defined, three one-second replicates were collected. In all cases, the
234 force-torque sensor's sampling rate was 1000 Hz.

235

236 **Flapping foil data processing**

237 The flapping-foil system generated time-series for pitch angle, heave amplitude, force,
238 and torque during each trial conducted. Since the pressure-based calculations were designed to
239 yield forces and torques acting on the foil, excluding the rod, a comparison could not be made
240 directly to the measurements from the flapping-foil apparatus, which could only measure from a
241 rod-foil assembly, or from the rod alone. So, to make an appropriate comparison, the forces and
242 torques from a given rod-only trial needed to be subtracted from the measured values from the
243 corresponding rod-foil assembly trial. This would isolate the forces and torques acting on the
244 foil. A custom Python (version 2.7.11, Python Software Foundation, <https://www.python.org>)
245 script was used to this subtraction in preparation for comparison with the calculated estimates,
246 yielding time-series of forces and torques due to solely the foil.

247 The script also applied a second-order Butterworth low-pass filter to the force and torque
248 data from the transducer. The filter was applied in two passes, to eliminate phase shifts, with a
249 desired cutoff frequency of 7 Hz (adjusted to 8.73 Hz in each pass to account for multiple passes)

250 [48]. This cutoff frequency was chosen through visual inspection as a compromise between
251 following the main trends and eliminating high frequency noise in the signals (e.g., Fig 3A).

252

253 **Fig. 3. Processing of highly repeatable measured force and torque data.**

254 Measured force data were highly repeatable. (A) Example raw and filtered lateral force (F_y)
255 traces, taken during dynamic testing. Three motion cycles during 1.0 Hz (top) and 2.0 Hz
256 (0° angle of attack motions are shown. (B) Filtered, phase-averaged traces of the data
257 from (A). Silhouettes represent standard deviations. Streamwise forces (F_x) and vertical torques
258 (T_z) followed similar trends to those displayed here.

259

260 Finally, the script performed phase-averaging of the three motion cycles, which
261 demonstrated that there was high repeatability in the measured force signals (Fig 3B).

262 All forces and torques were nondimensionalized using the following equations, where *
263 indicates a nondimensional term, F represents force, T represents torque, ρ is the density of fresh
264 water, c is foil chord, s is foil span, and v is the flow velocity.

265
$$F^* = \frac{F}{\rho s c v^2} \quad (5)$$

266
$$T^* = \frac{T}{\rho s c^2 v^2} \quad (6)$$

267

268 **Video data processing**

269 **Masking foils in video data**

270 A custom LabVIEW program [11] was used to automatically detect the foil as the largest,
271 brightest object in each video frame. Because the black rod did not contrast with the
272 background, the portion of the foil sandwiched by the 1-cm-wide rod was simulated as a 1-cm
273 straight line extending from the leading edge of the detected foil [11]. The automatically-
274 detected kinematics were then converted into mask boundaries, which would enclose vectors in

275 the velocity field to indicate to the pressure-algorithm the presence of a solid object. The mask
276 needed to be large enough to enclose the portion of the foil and rod below the light sheet which
277 blocked the view of flow within a few millimeters of the foil due to parallax effects (Fig 4A).
278 Mask-generation was accomplished in Matlab 2013b (MathWorks, Inc., Natick, MA, USA) by
279 plotting the detected foil as a white line on a black field (Fig 4B), and using binary image
280 dilation to widen the line by $1.1 \delta_{99}$ on each side, where δ_{99} is the 99% boundary layer thickness
281 (also called the shear-layer thickness). Boundary layer thickness was calculated using the
282 equation below, where x is foil chord length and Re is the Reynolds number [49].

$$283 \quad \frac{\delta_{99}}{x} = \frac{5}{\sqrt{Re}} \quad (7)$$

284 This dilation was enough to enclose velocity vectors inside the foil (Fig 4C). After the dilation,
285 200 equally-spaced coordinates on the black-white boundary were identified (Fig 4D). These
286 were smoothed with a 5-point-span moving average filter to generate the final mask (shaded area
287 in Figs 4E and 4F).

288

289 **Fig. 4. Image processing steps in making foil masks and force calculation boundaries.**

290 Boundary coordinates for foil masks and force calculation were generated using binary image
291 processing. (A)-(D) illustrate mask generation, and the same process was used to produce force
292 calculation boundaries. (A) A frame extracted from video of foil motion. Fluorescent paint at
293 the foil's midline appears as a bright line, and the portion of the foil below the light sheet is
294 visible due to parallax of 3D structures. (B) The automatically-detected midline of the foil. (C)
295 Binary image dilation widened the detected midline. (D) 200 equally-spaced points on the
296 black-white boundary in (C) were extracted to use as a mask enclosing both the foil's midline
297 and the portion of the foil visible below the light sheet. The points depicted here were smoothed
298 to remove jagged edges. (E) Smoothed foil mask plotted as a silhouette, and the 200-point force
299 calculation boundary produced by the same process. (F) Pressure contour for the video frame,
300 with the foil mask and force calculation boundary drawn in black.

301

302 **Particle image velocimetry**

303 DPIV analysis was conducted using DaVis 8.2.2 (LaVision GmbH, Goettingen, GER).

304 Any visible walls of the flow tank were masked. The cross-correlation analysis was conducted
305 in multiple passes with decreasing interrogation window sizes (32x32 and 16x16) and 50%
306 overlap. Two passes were made at each window size. During post-processing, vectors were
307 deleted if their correlation value was <0.8, though in some rare extremes, the cutoff was set at
308 0.6. The empty spaces were filled by interpolation, and simple 3x3 smoothing was applied to the
309 result, leading to a 128x128 grid of vectors. The use of this smoothing regime was motivated by
310 Wang et al.'s [50] findings. In their analysis of error level in pressure fields calculated from
311 velocity fields with known levels of Gaussian noise, they demonstrated that this average
312 smoothing of velocity fields reduced the noise level in pressure fields produced by the Dabiri et
313 al. [33] algorithm by 30-67% [50]. The flow velocity vector fields were exported for use with
314 the pressure algorithm.

315

316 **Nondimensionalization of vertical flow velocities**

317 The transverse DPIV fields revealed the vertical flow magnitudes (V_z) immediately to the
318 right of the foil as it approached direction reversal. To provide a measure of how important
319 vertical flows were relative to the horizontal (in-plane) flows at the same location, V_z was
320 normalized to a non-dimensional metric V_z^* ,

$$321 \quad V_z^* = \frac{V_z}{V_{tot}} \quad (8)$$

322 which represented the proportion of the total velocity magnitude at a given location that was in
323 the vertical direction. By assessing the *relative* importance of vertical flow, we would be able to
324 translate our analyses to other flows where the overall flow magnitude is different. Total
325 velocity magnitude (V_{tot}) was calculated using streamwise (V_x) and lateral (V_y) velocities from
326 the DPIV taken in the horizontal plane and vertical (V_z) velocities from the transverse plane.

327 This calculation was performed at every point of intersection of horizontal and vertical light
328 sheets, i.e., three positions on the rectangular foil's span, two positions on the tail-shaped foil's
329 span, as indicated by the bottom edge of the fluorescent paint strips in Fig 1. Means and
330 standard deviations of V_z^* from three replicate motion cycles were taken to provide a metric of
331 repeatability.

332

333 **Pressure-field algorithm**

334 Pressure fields were calculated using the Dabiri et al. [33] queen2 algorithm, which was
335 selected for its ability to handle the substantial body deformations characteristic of fish-like
336 swimming. In their paper, Dabiri et al. [33] described extensively the function and performance
337 of this pressure-field algorithm. In brief, the algorithm performs a direct integration of the
338 pressure gradient term of the Navier-Stokes equations along several paths through the field. To
339 reduce the effects of errors from individual paths, a median-polling scheme is used to choose the
340 estimate of pressure at every point in space. Dabiri et al. [33] validated their approach against
341 computational simulations of flow around a square cylinder and an anguilliform swimmer.
342 While Wang et al. [50] suggested that the Dabiri et al. [33] method favors speed over accuracy
343 compared to some other methods, the validations provided by Dabiri et al. [33] and the
344 subsequent experimental applications of the algorithm [51,52] indicate that it produces
345 sufficiently accurate fields to be useful in experimental studies.

346

347 **Selection of time-step for pressure calculation**

348 As the pressure-field algorithm reads in velocity data at some time interval (ex: once
349 every 0.01 s), a larger time step would be desirable to decrease computation times. To determine

350 what maximum time step between successive images would be permissible for high accuracy
351 results, multiple time steps – 0.01s, 0.004s, and 0.002s – were assessed for their viability (Fig 5).
352 Forces and torques were calculated using the pressure-based technique (following the methods in
353 the next section) for an arbitrarily-selected test case, the dynamic test’s 2.0 Hz trial in 0° angle of
354 attack motions. Smaller time steps permitted more high-frequency fluctuations into the traces
355 (Fig 5A). Because true trends can be revealed in measured data by using low-pass filtering to
356 eliminate high-frequency effects that are more sensitive to experimental error (see “Flapping foil
357 data processing” section), the same low-pass filter used on the sensor data was applied to the
358 traces calculated at 0.004s and 0.002s time steps. When plotted side-by-side, the filtered traces
359 resembled the trace produced with the 0.01s time step (Fig 5B). We confirmed that the 0.01s
360 time step was preserving the main trends in force and torque using a Fast Fourier Transform
361 analysis. Because the 0.01s yielded a reasonable time trace while significantly reducing
362 computational time, this value was selected for all subsequent force and torque calculations.

363

364 **Fig. 5. Time step selection for pressure field calculation.**

365 A comparison of the measured and calculated lateral force (F_y) values when the rectangular foil
366 was operating in 0° angle of attack motions at 2.0 Hz actuation frequency under different time-
367 steps. (A) The noise in the force trace from pressure-based force calculations decreased as time
368 step (ΔT) increased. (B) When a low-pass filter was applied to the noisy time traces, nearly
369 identical traces resulted, and these traces resembled the trace produced the time step was 0.01s.
370 Streamwise forces (F_x) and vertical torques (T_z) followed similar trends to those displayed here.
371

372 **Pressure-based force and torque calculation**

373 Pressure-based force and torque calculation was conducted based on the first terms in Eq.
374 1 and Eq. 2 in Matlab 2013b. Total force and torque were found as the sum of the force and
375 torque acting on a 200-point loop around the masked foil (Figs 4E and 4F). This force-

376 calculation loop was generated using the same binary image dilation procedure as was used for
377 the foil masks. A slightly larger dilation (discussed in the next paragraph) than before was
378 required to ensure that the calculation points were located where pressure was defined
379 (undefined within the mask) (Fig 4F). To calculate forces, pressure and the normal unit vector at
380 each of 200 dilated boundary points were noted, and the area term was calculated as the distance
381 between boundary coordinates times the span of the foil at the current boundary point. For
382 torque, the moment arm was defined as the perpendicular distances from the foil's leading edge.
383 Total forces and torques were nondimensionalized using Eq. 5 and 6.

384 Eq. 1 and 2 were formulated assuming that the control surface – the force calculation
385 loop from the previous paragraph – was drawn at the foil's surface, but, in practice, this loop
386 must be drawn at a small distance away from the foil. To determine how far away from the foil
387 the control surface could be placed before fluid terms must be added to Eq. 1 and 2 to maintain
388 accuracy, the force calculation process was conducted multiple times using the dynamic test's
389 2.0 Hz, 0° angle of attack trial as a test case. In each iteration, the control surface was drawn in a
390 new position. The binary image dilation process was used to place the control surface 1.5, 2.0,
391 2.5, 3.0, 3.5, and 4.0 δ_{99} from the foil's midline (Fig 6A). The resulting F_x^* and F_y^* time series
392 found in Fig 6B and 6C indicated that limited change to force magnitudes occurred until the
393 surface was placed $\sim 2.5\text{-}3.0 \delta_{99}$ away from the foil's midline. As such, we chose to draw the
394 final calculation boundaries by dilating the binary image in Fig 4B to a width of 15 pixels,
395 resulting in a loop $1.64 \delta_{99}$ from the foil's midline (Fig 6A). The decline observed here suggests
396 that additional fluid terms may be required in Eq. 1 and 2 for accurate force and torque
397 calculation when the calculation boundary is drawn far from the swimmer.

398

399 **Fig. 6. Forces calculated at different boundary positions.**

400 The magnitudes of the forces calculated using the pressure-based technique did not decline
401 substantially when the calculation loop was within ~ 2.5 boundary-layer-widths (δ_{99}) from the
402 foil's midline. To determine how close to the foil the force calculation loop needed to be for
403 high accuracy results, the pressure-based calculation was conducted on multiple loops around the
404 foil. Tests were conducted using pressure data from the dynamic, 2.0 Hz, 0° angle of attack trial.
405 Loop position was measured in δ_{99} -widths from the foil's midline. (A) All of the calculation
406 loops examined, drawn on the original image of the foil. (B) Non-dimensional streamwise forces
407 (F_x^*) for the different loops, over three periods of foil motion. (C) Non-dimensional lateral
408 forces (F_y^*) for the different loops, over three periods of foil motion.
409

410 **Metrics for comparing force and torque measurements and**
411 **estimations**

412 The estimated force and torque values derived from the pressure fields were compared to
413 the measured values from the flapping-foil system to determine their accuracy. Visual inspection
414 could reveal generally how well the two matched, but to quantify the match, three analyses were
415 conducted using a custom Python script. All quantitative comparisons were conducted based on
416 the three successive replicate traces (i.e., not the phased-averaged traces).

417 First, the correlation coefficient between each pair of corresponding measured and
418 estimated traces was calculated. This would demonstrate how well the shapes of the traces
419 matched. The limits of the 95% confidence interval for each correlation coefficient were
420 calculated to provide a measure of uncertainty in the correlation. The number of significant
421 figures was determined based on the standard error [53].

422 Next, to determine how well the magnitudes of the two traces matched, root mean square
423 error percentage (RMSE%) was calculated using the equations below, where M_i and C_i represent
424 corresponding force or torque values in the measured trace and calculated trace, respectively.

$$RMSE\% = \frac{\sqrt{\frac{\sum_{i=1}^n (M_i - C_i)^2}{n}}}{C_{max} - C_{min}} \times 100 = \frac{RMSE}{C_{max} - C_{min}} \times 100 \quad (9)$$

426

427 Finally, the presence of any phase lags was revealed using cross-correlation between
 428 corresponding measured and estimated time traces. The resulting lags were normalized by the
 429 duration of a motion cycle so as to facilitate comparisons.

430

431 **Depositing of data files and scripts**

432 All video and force-torque sensor data files are available from the “Video and sensor data
 433 for pressure-based force calculation validation” database on Harvard Dataverse available at
 434 <http://dx.doi.org/10.7910/DVN/5NCA5X>. The Dabiri et al. [33] pressure-field algorithm is
 435 available at <http://dabirilab.com/software/>. All other scripts used for data processing are
 436 available at <https://github.com/kelseynlucas>.

437

438 **RESULTS**

439 **Sensitivity of force and torque estimation to 3D flows**

440 Transverse imaging near the foils’ trailing edges revealed that fluid flow was
 441 predominantly in the horizontal plane for both the rectangular and the tail-shaped foils. The
 442 proportion, and hence, importance, of vertical flows relative to total flow (V_z^*) increased with
 443 proximity to the spanwise edges of the foil (Fig 7). The V_z^* magnitudes far from the foils’
 444 midlines were highly dependent on the size and strength of tip vortices attached to the spanwise
 445 edges of the foils (Fig 7). The largest V_z^* observed was 35%, when the rectangular foil was
 446 moved in the 0° angle of attack program. Vertical velocity (V_z) traces were more complex for the

447 tail-shaped foil than for the rectangular foil, as a result of interactions between the upstream
448 “body” and downstream “tail” portions of this foil. In particular, tip vortices shed from the body
449 portion of the foil upstream are visible on the right side of the flow field in Fig 7C.

450

451 **Fig. 7. Velocity vector fields in the transverse plane.**

452 Velocity vector fields in the transverse plane as the foils approach direction reversal, for 1.5 Hz
453 actuation frequency, 1.5 cm heave amplitude, and 30 cm/s oncoming flow (the conditions used
454 for 3D testing). The foils move toward the left. Vertical velocities (V_z) were taken along a
455 vertical line immediately to the right of the foil. Bright spots represent either the edges of the
456 foil or the strips of fluorescent paint. Colors in velocity traces represent different trials. (A)
457 Rectangular foil, 0° angle of attack program. (B) Rectangular foil, heaving program. (C) Tail-
458 shaped foil, 0° angle of attack program. (D) Tail-shaped foil, heaving program. $V_z^* - V_z$
459 normalized by the total velocity at the measurement location, plus or minus standard deviation.
460 Rect – rectangular foil. Tail – tail-shaped foil.

461

462 During the 3D tests, the agreement between the measured force and torque values from
463 the flapping-foil system and the predictions based on the pressure fields was, in the majority of
464 cases, exceptional. For lateral forces (F_y) and torques about the vertical axis (T_z), typical
465 correlation coefficients for both foils were greater than 0.9, with typical RMSE% less than 25%,
466 and phase lags less than 5% (Tables 1 and 2). The exceptions to these trends generally were
467 localized to the foils’ spanwise edges, and, as discussed later, these exceptions can point to
468 where the limitations of this method lie. These high, positive correlation coefficients, low
469 RMSE%, and limited phase lags respectively demonstrate that the pressure-based calculation
470 was able to reproduce the shape, magnitude, and timing of the locomotor forces and torques
471 acting on the foils even when the magnitude of vertical flows became more substantial (Figs 8
472 and 9). Additionally, where the calculated values deviated from the measurements, the
473 calculations tended to underestimate the true values (Figs 8 and 9).

474 **Table 1. Rectangular foil – quantitative comparisons^a of forces and torques from three-dimensional tests.**

475

Motion type	Laser position	Correlation Coefficient ^b (95% CI low, high)			RMSE%			Phase Lag % ^c		
		F_x	F_y	T_z	F_x	F_y	T_z	F_x	F_y	T_z
0angle	Midline ^d	0.963 (0.951, 0.972)	0.937 (0.917, 0.952)	0.9924 (0.9899, 0.9942)	30.3	12.7	7.3	0	1.5	0
	2 cm	0.985 (0.980, 0.989)	0.982 (0.976, 0.986)	0.9972 (0.9963, 0.9979)	15.9	12.2	10.1	0	3	0
	Edge	0.935 (0.915, 0.950)	0.989 (0.985, 0.991)	0.984 (0.978, 0.988)	30.3	30.5	25.4	-1.5	0	-1.5
heave	Midline	0.341 (0.212, 0.459)	0.976 (0.969, 0.982)	0.987 (0.983, 0.990)	45.8	8.2	7.7	9	-1.5	0
	2 cm	0.523 (0.414, 0.617)	0.968 (0.958, 0.976)	0.978 (0.971, 0.983)	51.3	13.4	12.1	-48	-3.0	-1.5
	Edge	0.355 (0.227, 0.471)	0.765 (0.701, 0.818)	0.942 (0.924, 0.956)	55.4	45.2	14.3	-57	-10.5	-1.5

476

477 0angle = 0° angle of attack motions; heave = heaving motions; 95% CI = confidence interval; RMSE% = root-mean-square error percentage.

478 ^a Note that some quantitative analyses performed poorly at low force magnitudes and may therefore underestimate the agreement between the measured and
479 calculated force and torque values. See Results section in the main text for details.

480 ^b Normalized values.

481 ^c Phase lags, as percentages of motion cycle periods, were determined by cross-correlation.

482 ^d Due to unusual oscillations resulting from a loose screw, midline data were replaced with equivalent data from dynamic testing.

483

484

485 **Table 2. Tail-shaped foil – quantitative comparisons^a of forces and torques from three-dimensional tests.**

486

Motion type	Laser position	Correlation Coefficient ^b (95% CI low, high)			RMSE%			Phase Lag % ^c		
		F_x	F_y	T_z	F_x	F_y	T_z	F_x	F_y	T_z
0angle	Midline	0.949 (0.933, 0.961)	0.924 (0.900, 0.942)	0.970 (0.961, 0.977)	50.2	21.8	24.1	0	3	1.5
	Gap	0.887 (0.853, 0.913)	0.963 (0.951, 0.972)	0.969 (0.959, 0.976)	43.9	33.6	20.6	-3	-1.5	-3
heave	Midline	0.424 (0.303, 0.532)	0.924 (0.900, 0.942)	0.932 (0.911, 0.948)	43.0	22.7	12.5	-7.5	-4.5	3
	Gap	0.723 (0.649, 0.783)	0.983 (0.977, 0.987)	0.940 (0.922, 0.955)	36.8	11.9	22.8	0	-1.5	0

487

488 0angle = 0° angle of attack motions; heave = heaving motions; 95% CI = confidence interval; RMSE% = root-mean-square error percentage.

489 ^a Note that some quantitative analyses performed poorly at low force magnitudes and may therefore underestimate the agreement between the measured and
 490 calculated force and torque values. See Results section in the main text for details.

491 ^b Normalized values.

492 ^c Phase lags, as percentages of motion cycle periods, were determined by cross-correlation.

493

494 **Fig. 8. Results of three-dimensional testing of the rectangular foil.**

495 Comparisons of phase-averaged ($n=3$) measured and calculated force and torque time traces
496 reveal that the pressure-based force calculation was generally able to accurately reproduce both
497 the shape and magnitude of the measured trace, although the agreement declined with proximity
498 to the foil's edge. (A) Results from 0° angle of attack motions. Due to unusual oscillations
499 resulting from a loose screw, midline data were replaced with equivalent data from dynamic
500 testing. (B) Results from heaving motions. F_x – streamwise forces. F_y – lateral forces. T_z –
501 torques about the vertical axis. Foil kinematics corresponded with the 1.5 Hz cases in dynamic
502 testing (see Figs 10 and 11). Silhouettes represent standard deviations.

504 **Fig. 9. Results of three-dimensional testing of the tail-shaped foil.**

505 Despite the more complex shape of this foil, the pressure-based calculations were often able to
506 accurately reproduce both the shape and the magnitude of the measured time traces. (A)
507 Comparisons of phase-averaged ($n=3$) measured and calculated time traces. (B) Midline
508 kinematics over one motion cycle. F_x – streamwise forces. F_y – lateral forces. T_z – torques about
509 the vertical axis. St – Strouhal number. Silhouettes represent standard deviations.

511 In all of the 3D tests performed, absolute F_x magnitudes were quite small – <0.2 N, or
512 <0.3 nondimensionalized, compared to <0.8 N or <0.6 nondimensionalized for F_y (Figs 8 and 9),
513 and the pressure-based force calculation was able to reproduce these small magnitudes. Yet,
514 while F_x correlation coefficients were in excess of 0.85 in all but one case in the 0° angle of
515 attack program, the values in the heaving program were about 0.3-0.5 for the rectangular foil and
516 0.4-0.7 for the tail-shaped foil (Tables 1 and 2). For both foils in both programs, typically, the
517 RMSE% ranged from 15-55%, with phase lags between 0-60% (Tables 1 and 2). To resolve this
518 discrepancy, we must note that because F_x magnitudes were small, slight deviations between the
519 estimated and measured time traces would translate to large percent differences. For this reason,
520 the RMSE% of streamwise forces reported in Tables 1 and 2 are somewhat misleading.
521 Likewise, phase lags hold little meaning when the correlation between two signals is limited.

522 The misleading nature of the quantitative analyses for small force magnitudes also
523 becomes apparent from the size scales of the 95% confidence intervals for the correlation

524 coefficients (Tables 1 and 2). While the “95% confidence interval” merely means that we are
525 95% sure that the true correlation coefficient is within the given range, the size of the range can
526 provide a proxy for how uncertain the reported values are. Here, the 95% confidence intervals
527 for the F_x correlation coefficient were 50% to an order of magnitude larger than for those for F_y
528 or T_z , particularly where the F_x correlation coefficients were less than 0.8 (Tables 1 and 2). This,
529 again, indicated that some of the quantitative analyses perform poorly where force magnitudes
530 were small. The remainder, however, including the difference in correlation coefficients
531 between 0° angle of attack cases where $F_x^* < 0.3$ nondimensionalized and heaving cases where
532 $F_x^* < 0.08$ nondimensionalized, can reveal some insight into how well this force calculation
533 method will work for studies of biological locomotion, as discussed in later sections.

534

535 **Sensitivity of force and torque estimation to flapping frequency**

536 The overall trends resulting from dynamic testing were similar to those from the 3D tests.
537 With one exception, the F_y and T_z correlation coefficients were >0.85 . The RMSE% was
538 generally $<20\%$, and phase lags were minimal at $<6\%$ (Table 3). The lowest flapping frequency,
539 0.5 Hz, generally had the poorest agreements among the dynamic tests with slightly smaller
540 correlation coefficients and slightly larger RMSE% and phase lags than the higher frequencies.
541 Again, F_x results were more inconsistent. At all but the lowest frequency, agreements in the 0°
542 angle of attack motion program were better than the heaving program: higher correlation
543 coefficients, lower RMSE%, and smaller phase lags (Table 3). Yet, as in the 3D tests, large 95%
544 confidence intervals (Table 3), a high level of agreement between time-traces in the
545 visualizations (Figs 10 and 11), and low absolute F_x magnitudes (compare <0.5 N or <0.4
546 nondimensionalized in 0° angle of attack trials to <0.1 N or 0.08 nondimensionalized in the

547 heaving trials) indicated that the quantitative metrics were misleading due to the low
548 performance of the analyses at small force magnitudes. As in the 3D tests, though, these results
549 can still suggest where the limits to the pressure-based calculation method are for the study of
550 biological locomotion, as discussed in later sections.

551

552 **Fig. 10. Results of dynamic testing, 0° angle of attack motions, of the rectangular foil.**

553 Generally, the pressure-based calculations were able to accurately reproduce both the shape and
554 the magnitude of the measured time traces. Agreement declined slightly as actuation frequency
555 increased. (A) Comparisons of phase-averaged (n=3) measured and calculated time traces. (B)
556 Midline kinematics over one motion cycle, corresponding to the time traces on the left. F_x –
557 streamwise forces. F_y – lateral forces. T_z – torques about the vertical axis. St – Strouhal number.
558 Silhouettes represent standard deviations.

559

560 **Fig. 11. Results of dynamic testing, heaving motions, of the rectangular foil.**

561 Generally, the pressure-based calculations were able to accurately reproduce both the shape and
562 the magnitude of the measured time traces, but less so than during 0° angle of attack motions.
563 Agreement declined slightly as actuation frequency increased. (A) Comparisons of phase-
564 averaged (n=3) measured and calculated time traces. (B) Midline kinematics over one motion
565 cycle, corresponding to the time traces on the left. F_x – streamwise forces. F_y – lateral forces. T_z
566 – torques about the vertical axis. St – Strouhal number. Silhouettes represent standard
567 deviations.

568

569 **Table 3. Dynamic tests – quantitative comparison^a of forces and torques at increasing actuation frequencies.**
570

Motion type	Freq [Hz]	Correlation Coefficient ^b (95% CI low, high)			RMSE%			Phase Lag % ^c		
		F_x	F_y	T_z	F_x	F_y	T_z	F_x	F_y	T_z
0angle	0.5	0.248 (0.171, 0.322)	0.908 (0.893, 0.921)	0.914 (0.900, 0.926)	165.5	24.3	10.9	50	0.5	-1.0
	1.0	0.870 (0.840, 0.895)	0.992 (0.990, 0.994)	0.9914 (0.9893, 0.9932)	53.6	13.2	8.0	0	0	0
	1.5	0.963 (0.951, 0.972)	0.972 (0.962, 0.978)	0.9924 (0.9899, 0.9942)	30.3	12.7	7.3	0	1.5	0
	2.0	0.948 (0.929, 0.962)	0.971 (0.960, 0.979)	0.9947 (0.9926, 0.9961)	16.8	10.4	5.9	0	0	0
	2.5	0.929 (0.889, 0.950)	0.792 (0.713, 0.851)	0.9942 (0.9916, 0.9960)	14.7	19.5	6.4	0	0	0
heave	0.5	0.513 (0.451, 0.569)	0.869 (0.848, 0.888)	0.649 (0.601, 0.693)	279.2	28.9	21.7	1.5	0	-1.5
	1.0	0.605 (0.528, 0.672)	0.981 (0.976, 0.985)	0.956 (0.945, 0.965)	165.6	12.4	10.7	2.0	0	-1.0
	1.5	0.152 (0.013, 0.286)	0.883 (0.848, 0.910)	0.956 (0.942, 0.966)	82.0	15.9	8.3	10.5	-6.0	-1.5
	2.0	0.063 (-0.099, 0.222)	0.891 (0.852, 0.920)	0.958 (0.942, 0.969)	57.0	17.5	9.8	-86	-6.0	-2.0
	2.5	0.556 (0.417, 0.669)	0.988 (0.983, 0.992)	0.856 (0.799, 0.898)	36.8	18.3	15.9	2.5	0	-5.0

571
572 0angle = 0° angle of attack motions; heave = heaving motions; Freq = frequency; 95% CI = confidence interval; RMSE% = root-mean-square error percentage.
573 ^a Note that some quantitative analyses performed poorly at low force magnitudes and may therefore underestimate the agreement between the measured and
574 calculated force and torque values. See Results section in the main text for details.
575 ^b Normalized values.
576 ^c Phase lags, as percentages of motion cycle periods, were determined by cross-correlation.

577 The RMSE% values, alongside the visualizations in Figs 10 and 11, indicated that the
578 agreement between the direct measurements and pressure-based estimates was best at moderate
579 flapping frequencies and poorest at the extremes. These moderate frequencies are close to the
580 frequencies where the rectangular foil achieves self-propelled speed – the speed where net forces
581 and torques over a motion cycle are zero (occurs at 1.0 Hz during 0° angle of attack motions, 1.5
582 Hz during heaving motions) [11]. Even so, the generally high level of agreement indicated that
583 this method of pressure-based estimation of locomotor forces and torques will perform well for a
584 swimmer in steady, accelerating, and decelerating motion, provided the swimmer is not
585 moving particularly slowly – e.g., the 0.5 Hz flapping frequency case, which is at the lower
586 extreme of tailbeat frequencies used by fish [16,46,47].

587

588 **Results from static testing**

589 As anticipated, when the foil was held statically and viscous effects were relatively more
590 important than pressure effects, the pressure-based estimates of forces and torques were very
591 poor (Fig 12). Correlation coefficients clustered around zero, and there was no consistent trend
592 in RMSE% (Table 4). In particular, the pressure-based calculation was unable to detect any drag
593 on the foil, though the measurements consistently revealed negative F_x (Fig 12).

594

595 **Fig. 12. Results of static testing of the rectangular foil.**

596 In the static case, where shear forces dominate, the pressure-based calculations were not able to
597 accurately predict locomotor forces and torques. For the comparisons of phase-averaged (n=3)
598 measured and calculated time traces, note that the y-axis scales vary among oncoming flow
599 speeds and differ from those in other figures. F_x – streamwise forces. F_y – lateral forces. T_z –
600 torques about the vertical axis. Silhouettes represent standard deviations.

601

602 **Table 4. Static tests – quantitative comparison of forces and torques at increasing**
 603 **oncoming flow speeds.**

604

Flow speed [cm/s]	Correlation Coefficient ^a (95%CI low, high)			RMSE%		
	F_x	F_y	T_z	F_x	F_y	T_z
10	-0.117 (-0.227, -0.003)	-0.132 (-0.242, -0.018)	-0.016 (-0.129, 0.098)	44.6	34.6	29.9
30	0.080 (-0.034, 0.192)	0.127 (0.014, 0.237)	0.170 (0.057, 0.278)	82.8	19.7	19.6
50	0.001 (-0.112, 0.115)	0.588 (0.508, 0.658)	0.278 (0.170, 0.379)	98.0	27.1	19.5

605
 606 95% CI = confidence interval; RMSE% = root-mean-square error percentage.
 607 ^aNormalized values.

608

609 **Discussion**

610 Many of the diverse morphological features of fishes are tied to swimming behaviors, and
 611 consequently, understanding a fish’s locomotion is an integral part of answering many
 612 unresolved questions about evolution and function in fishes. The ability to use standard 2D
 613 DPIV data to calculate the instantaneous distribution of forces and torques on freely-swimming
 614 fishes would represent a substantial advance in our ability to study aquatic locomotion. Hence,
 615 we propose a pressure-based method for obtaining this information non-invasively and focus
 616 here on validating this approach and determining the experimental conditions under which it
 617 works best. Our comparisons of the forces and torques estimated through pressure-based
 618 calculations to the values measured by a load cell revealed that, under many conditions, the
 619 pressure-based calculation was able to accurately estimate time-dependent locomotor forces and
 620 torques. We were often able to reproduce the shape, magnitude, and timing of the measured
 621 traces.

622 The points at which the pressure-based calculations led to low accuracy force and torque
 623 estimations suggest where the limits of this approach for biological study lie. Largely, the key
 624 factors responsible for the method’s performance were based on the validity of the assumptions

625 behind the technique: 1) that the fluid velocity perpendicular to the horizontal imaging plane is
626 relatively small, an assumption inherent to 2D DPIV [40], and 2) that the Reynolds number is
627 sufficiently high such that the pressure (inertial) term in Eq. 1 and 2 dominates the shear
628 (viscous) term. In the following sections, we leverage our data on the relative roles of horizontal
629 vs. out-of-plane flows and the pressure vs. shear effects to explain where the limits of this
630 pressure-based approach to force and torque calculation lie for biological locomotion studies.
631 We find that where a given trial falls on each of these spectra together determines the accuracy
632 of the calculation.

633 Notably, the agreement between measured and estimated force and torque values was
634 best during 0° angle of attack motions, a kinematic regime more similar to the motions used by a
635 swimming fish [11,15]. Moreover, the agreement for streamwise – thrust or drag – forces was at
636 its best in this program at higher flapping frequencies (Figs 10 and 11; Table 3), which
637 correspond more closely to typical tailbeat frequencies used by fish [16,46,47], and additionally,
638 the agreement was strong close to the foils' spanwise edges (Figs 8 and 9; Tables 1 and 2). This
639 points to the especial utility and promise of this force and torque estimation procedure for studies
640 of biological swimming.

641

642 **Limitations due to 2D methodology**

643 As a whole, the effectiveness of the pressure-based force and torque estimation using the
644 first terms in Eq. 1 and 2 was highly dependent on the quality of the DPIV data. While factors
645 such as temporal and spatial resolution and DPIV uncertainty do affect the outcome, their effects
646 can easily be addressed using good imaging technique – e.g., those outlined by Stamhuis and
647 Videler [40] and de Kat and van Oudheusen [54] – and post-hoc smoothing of velocity fields

648 [50]. Less apparent, however, are the limitations posed by using a 2D plane to characterize a
649 flow through a 3D space. Yet, this approach is often the most feasible option in biological
650 studies that measure locomotor flows.

651 While flows around a real, 3D object will inherently have some degree of three-
652 dimensionality, in many cases, a 2D analysis can provide sufficient information to answer the
653 questions posed in a given experiment – for example, Drucker and Lauder [17]. How we decide
654 whether 2D analysis is sufficient is, to some extent, subjective, but the 3D tests on the
655 rectangular and tail-shaped foils demonstrate that some degree of deviation from the 2D
656 assumption will still lead to fairly accurate results (Figs 8 and 9).

657 We found that proximity to the edge of the rectangular foil, where the relative magnitude
658 of vertical flows (V_z^*) was greatest, was associated with poorer force and torque predictions (Fig
659 7; Table 1). The pattern of the decline did not vary substantially between motion programs
660 (Table 1). The exception was lateral force (F_y) at this foil's edge, which saw a large increase in
661 error only in the heaving program (Table 1). It is likely that the sweep of fluid around the edge
662 of the foil as it heaved laterally (Fig 7) reduced the build-up of pressure gradients near the edge,
663 underestimating the gradients at other locations along the foil's span. This effect on F_y would be
664 more profound in the heaving program where the majority of the foil's surface area faces
665 laterally (Fig 11B). Thus, the pressure-based forces also primarily point laterally.

666 Another key observation from the rectangular foil is that the agreement between
667 estimated and measured force and torque traces was generally better during the 0° angle of attack
668 than during the heaving program (Table 1). The explanation is straightforward. When this foil is
669 moved in heave, a strong leading edge vortex forms, leading to a low pressure peak (Figs 13 and
670 14). During direction reversal, this vortex is shed and begins to travel downstream, and is

671 subsequently impacted by the foil (Figs 13 and 14). The resulting complex flow persists through
672 the next motion cycle and affects approximately the first 40% of the foil's length (Figs 13 and
673 14), and likely has significant vertical components. While this does lead to large pressure
674 magnitudes in the horizontal plane (Fig 14), the 2D visualization does not capture the vertical
675 effects, leading to underestimates of forces and torques. It is worth noting that these transient but
676 potentially highly 3D flows also affect estimations at the highest flapping frequencies studied,
677 where direction reversals, and hence, vortex impacts, occur more often. This is apparent in the
678 slight decline in estimation accuracy during these tests (Figs 10 and 11; Table 3). In contrast, the
679 poor agreements at low frequencies can be attributed to shear, as discussed in later sections.

680

681 **Fig. 13. Velocity vector fields in the horizontal plane, at the foil's midline.**

682 Velocity vector fields at the foils' midlines revealing the differences in flow structures around
683 the rectangular (Rect) and tail-shaped (Tail) foils during 0° angle of attack and pure heaving
684 motions at three points in a stroke cycle. The foils were moved at 1.5 Hz actuation frequency
685 and 1.5 cm heave amplitude, in an oncoming flow of 30 cm/s. Before direction reversal, the foils
686 move downward. While flow moves smoothly along the foils during 0° angle of attack motions,
687 in the heaving program, a leading edge vortex is formed, shed, and destroyed in the succession of
688 images.

689

690 **Fig. 14. Pressure fields in the horizontal plane, at the foil's midline.**

691 Pressure fields at the foils' midlines around the rectangular (Rect) and tail-shaped (Tail) foils
692 during 0° angle of attack and pure heaving motions at three points in a stroke cycle,
693 corresponding to the snapshots in Fig 13. The foils were moved at 1.5 Hz actuation frequency
694 and 1.5 cm heave amplitude, in an oncoming flow of 30 cm/s. Before direction reversal, the foils
695 move downward. Color bar indicates the coefficient of pressure (C_p). During 0° angle of attack
696 motions, pressure gradients peak near the trailing edge. In the heaving program, pressure peaks
697 in the leading edge vortex, and deteriorates into complex patterns as the vortex is impacted by
698 the foil.

699

700 Unlike the heaving program, the 0° angle of attack motion sweeps fluid smoothly and
701 accelerates it along the foil's length without forming a leading edge vortex or pressure peak (Figs

702 13 and 14). This smooth flow and acceleration indicates that the tip vortices are entraining fluid
703 and increasing in strength along the entirety of the foil's length before being shed near the
704 trailing edge, rather than being distorted through interaction with leading edge vortices. Thus,
705 for the rectangular foil in the 0° angle of attack program, the relative contribution of out-of-plane
706 flows (V_z^*) measured near the foil's trailing edge (Fig 7) represent maximums. The limited
707 importance of vertical flows in this program (<35%) ensures that the 2D assumptions are valid,
708 and so the estimation is successful.

709 The trends of force estimation success were somewhat different for the tail-shaped foil
710 (Fig 9; Table 2). At the foil's midline, the estimation was marginally better in the 0° angle of
711 attack program, as observed in the rectangular foil. But, when the laser was positioned to cross
712 the foil's gap, the results were approximately the same in the two motion programs.

713 The flow visualizations (Figs 7, 13, and 14) shed some light – the more complex foil
714 shape led to more complicated fluid interactions. This foil's shape, particularly the narrowing of
715 the body into the peduncle, entrains fluid into tip vortices that are angled up or down, following
716 the body, rather than aligned horizontally as in the rectangular foil (Fig 7). The resulting large
717 vertical effects are compounded by the 0° angle of attack kinematics, where the foil sweeps
718 through greater lateral excursions (Fig 9B) [11,15], which further accelerates fluid along the foil
719 (Fig 13). This greatly strengthens the tip vortices attached to the foil's body and amplifies the
720 vertical flows, until these vortices are shed anterior to the peduncle. These shed vortices are
721 visible on the right side of Fig 7C, and appear to interact with the new tip vortices developing on
722 the foil's tail region. When the horizontal laser was positioned so as to cross the gap in the foil,
723 the light sheet intersected both these complex flows in the tail region and the strong vertical
724 flows in the body region (Figs 7, 13 and 14), leading to a reduction in accuracy of the force

725 estimation. Note that, as the transverse light sheet was positioned posterior to the peduncle, the
726 V_z^* values in Figs 7C and 7D are underestimates of the vertical velocities on the foil as a whole.
727 In contrast, the foil experiences less lateral excursion in the heaving program (Fig 9B) and
728 weaker tip vortices, which are not shed or have dissipated upstream of the transverse light sheet
729 position (Fig 7D), so the relative importance of vertical flows – and the deviation from the 2D
730 assumption – is minimal. Thus, when the horizontal laser is positioned at the gap in the heaving
731 program, the force estimation accuracy does not decline.

732 Generally, though, we observed high correlation, limited phase shifting, and low error
733 percentage (Tables 1 and 2), as well as the reproduction of general trends such as increasing
734 forces and torques with flapping frequency (Figs 10 and 11). These observations indicate that,
735 where the 2D assumption behind DPIV is valid – e.g., vertical flows are less than ~30% of the
736 total velocity magnitude at any given point (Fig 7) – the 2D pressure-based calculation will be
737 sufficient to provide reasonable estimates of locomotor forces and torques. It is likely that this
738 will also be true in the event of slightly larger V_z^* s, which may be experienced in the anterior
739 50% of the rectangular foil during heaving motions and of the tail-shaped foil during 0° angle of
740 attack motions, but were not captured at the given transverse light sheet position.

741

742 **Role of pressure vs shear effects**

743 Pressure-based force and torque calculations rely on the assumption that the shear terms
744 in Eq. 1 and 2 are small relative to the pressure terms, and hence, the shear terms can be ignored
745 without greatly affecting the accuracy of the result. This assumption is typically met for fish-like
746 swimmers operating at high enough Re. Moreover, Bale et al. [27] suggest that the pressure and
747 shear terms are inversely related: when one is large, the other is small. We illustrate this tradeoff

748 in an extreme with data from the static case. Here, pressure effects (first term in Eq. 1 and 2) are
749 minimal and shear effects (second term in Eq. 1 and 2) dominate: pressure-based calculations
750 alone are unable to estimate the forces and torques experienced by the foil (Fig 12; Table 4).

751 The tradeoff between shear and pressure effects, however, implies that a middle ground
752 exists where both effects moderately contribute to the total forces. Here, the values calculated
753 from the first terms in Eq. 1 and 2 might provide a good, but not perfect, estimation of true forces
754 and torques. The question is, where does this middle ground fall during fish-like locomotion?

755 The dynamic test results offer some insight on this point. Agreement between the
756 measurements and the pressure-based estimations improved with flapping frequency (until the
757 3D effects described in the previous section caused a decline), and was better in the 0° angle of
758 attack program than the heaving program (Figs 10 and 11; Table 3).

759 While the large errors in F_x were in part due to the small absolute force magnitudes –
760 small magnitude deviations therefore translated to large percent changes – the relatively low
761 level of agreement in F_x versus the higher level of agreement for F_y and T_z suggest that the
762 accuracy of estimation is dependent on the relative proportion of pressure versus shear effects on
763 a given axis.

764 Two key facts lead to this idea: first, pressure forces act normal to a surface, and second,
765 the majority of the surface area of our foil models – essentially flat plates – faces laterally (Figs
766 9B, 10B, and 11B), normal or nearly normal to the axis of progression during swimming. Thus,
767 on the lateral axis, the large pressure-based contribution dominates the shear effects, so the force
768 estimation performs well. In contrast, the much smaller surface area facing in the streamwise
769 direction leads to a small pressure-based contribution that cannot dominate the shear forces.
770 Instead, the shear term in Eq. 1 is relatively large, and so a purely pressure-based force

771 calculation yields an underestimate of F_x . This effect is magnified as less surface area is aligned
772 axially, as in motions where the foil experiences limited bending – i.e., heaving motions, and at
773 low frequencies (Figs 10B and 11B). The static foil cases (Fig 12), moreover, could be
774 considered an extreme example of this effect and show some of the poorest F_x predictions. At
775 the other extreme are the results for the dynamic test at 2.5 Hz, the highest frequency tested, in
776 the 0° angle of attack program (Fig 10). The high degree of foil bending here leads to the largest
777 streamwise-facing surface area, and the best F_x and poorest (relatively speaking; the correlation
778 coefficient was 0.792) F_y estimates observed (Fig 10; Table 3).

779 Unlike flat plates, biological swimmers have greater thickness, and hence, more axial
780 surface area. In addition, head oscillation, common in swimming fishes [7,55], results in a
781 substantial contribution to the streamwise-facing surface area. Fish also tend to follow a
782 kinematic regime more similar to the 0° angle of attack program [11,15], which increases
783 bending (Figs 10B and 11B), and again, axially-oriented surface area. Thus, while we would
784 predict that the relative proportion of surface area can provide an idea of how well pressure-
785 based force estimation will perform on a given axis, it is likely that for many biological
786 swimmers, this pressure-based force and torque estimation method will provide reasonable
787 values in both the lateral and streamwise directions.

788

789 **Implications for fish locomotion studies**

790 Together, the 3D and dynamic tests illustrate how 1) the relative importance pressure
791 versus shear and 2) the 3D effects both are factors affecting the accuracy of the force and torque
792 calculations. Moreover, as we have described in the proceeding sections, these two factors
793 appear to have opposing effects relative to the actuation frequency. That is, the maximum

794 frequency (2.5 Hz) and the minimum frequency (0.5 Hz) both led to less accurate outcomes than
795 the moderate frequencies in between. Yet, the decline in performance at the lowest frequency
796 due to shear was much more substantial than the impact of 3D flows at the highest frequency.
797 This is consistent with the main assumption behind our method of force and torque calculation –
798 the assumption that allowed the simplification of Eq. 1 and 2, namely, that the pressure effects
799 are large relative to the shear effects.

800 Notably, the pure heaving motions are less biologically realistic [11,15] than the 0° angle
801 of attack motions which also increase bending along the foil's length and the effective axial
802 surface area. The 0° angle of attack motions additionally eliminate the vortex impacts that led to
803 substantial out-of-plane flow in the heaving program. The lowest frequencies tested here, while
804 within the range of tailbeat frequencies used by fish [16,46,47], correspond to the lower extreme
805 of this range. Thus, it appears that, during typical fish-like locomotion, represented here by
806 higher frequencies and 0° angle of attack motions, the pressure effects dominate the shear effects
807 and the 3D effects are sufficiently small, and so the pressure-based estimation of locomotor
808 forces and torques will perform well.

809

810 **Conclusion**

811 Here, we described an experimental method for obtaining time-varying swimming force
812 and torque data using standard 2D DPIV in conjunction with a pressure field algorithm. Using a
813 mechanical flapping foil apparatus that models fish-like swimming and simultaneous DPIV
814 video collection and subsequent calculations, we characterized the conditions where this
815 approach is expected to work well. We demonstrated that this technique is often able to
816 accurately reproduce the shape, magnitude, and timing of locomotor forces and torques

817 experienced by a fish-like swimmer.

818 Detailed knowledge of the time-varying forces and torques acting on a fish's body is a
819 key component of answering many unresolved questions about form and function in fish, but
820 these data are difficult to measure with the necessary detail and while allowing the animal to
821 swim freely. Our results indicate that pressure-based methods such as that studied here can
822 readily provide the missing detailed, instantaneous force and torque information that, in the past,
823 precluded a more comprehensive understanding of biological swimming.

824

825 **Acknowledgements**

826 This work was supported by a National Science Foundation Graduate Research Fellowship under
827 grant DGE-1144152 and a Harvard University Chapman Fellowship to KNL and by the Office of
828 Naval Research Multi-University Research Initiative Grant N000141410533 monitored by Dr.
829 Bob Brizzolara to GVL. The funders had no role in study design, data collection and analysis,
830 decision to publish, or preparation of the manuscript. Thanks to Francis Carr, Ryan Feather,
831 Patrick Thornycroft, Brad Gemmell, and Eric Tytell for technical assistance, and to Iman
832 Borazjani, Kara Feilich, Elena Kramer, and Pete Girguis for helpful discussions. We also thank
833 Eric Tytell, Sean Colin, and the anonymous reviewers for their feedback on earlier versions of
834 this manuscript. The authors declare that no competing interests exist.

835

References

- [1] Lighthill MJ. Hydromechanics of aquatic animal propulsion. *Annu Rev Fluid Mech* 1969;1:413–46.
- [2] Weihs D, Webb PW. Optimization of Locomotion. In: Webb PW, Weihs D, editors. *Fish Biomech.*, New York: Praeger Publishers; 1983, p. 339–71.
- [3] Blake RW. Fish functional design and swimming performance. *J Fish Biol* 2004;65:1193–222. doi:10.1111/j.1095-8649.2004.00568.x.
- [4] Domenici P, Kapoor BG. *Fish locomotion: an eco-ethological perspective*. Boca Raton, FL: CRC Press; 2010.
- [5] Webb PW. Body form, locomotion and foraging in aquatic vertebrates. *Integr Comp Biol* 1984;24:107–20.
- [6] Feilich KL. Correlated evolution of body and fin morphology in the cichlid fishes. *Evolution (N Y)* 2016;70:2247–67. doi:10.1111/evo.13021.
- [7] McHenry MJ, Pell CA, Long JH. Mechanical control of swimming speed: stiffness and axial wave form in undulating fish models. *J Exp Biol* 1995;198:2293–305.
- [8] Long JH. Muscles, elastic energy and the dynamics of body stiffness in swimming eels. *Am Zool* 1998;38:771–92. doi:10.1093/icb/38.4.771.
- [9] Tytell ED, Hsu C-Y, Williams TL, Cohen AH, Fauci LJ. Interactions between internal forces, body stiffness, and fluid environment in a neuromechanical model of lamprey swimming. *Proc Natl Acad Sci U S A* 2010;107:19832–7. doi:10.1073/pnas.1011564107.
- [10] Lucas KN, Johnson N, Beaulieu WT, Cathcart E, Tirrell G, Colin SP, et al. Bending rules for animal propulsion. *Nat Commun* 2014;5. doi:10.1038/ncomms4293.
- [11] Lucas KN, Thornycroft PJM, Gemmell BJ, Colin SP, Costello JH, Lauder GV. Effects of non-uniform stiffness on the swimming performance of a passively-flexing, fish-like foil model. *Bioinspir Biomim* 2015;10:56019. doi:10.1088/1748-3190/10/5/056019.
- [12] Standen EM, Lauder GV. Hydrodynamic function of dorsal and anal fins in brook trout (*Salvelinus fontinalis*). *J Exp Biol* 2007:325–39.
- [13] Borazjani I, Sotiropoulos F. On the role of form and kinematics on the hydrodynamics of self-propelled body/caudal fin swimming. *J Exp Biol* 2010;213:89–107. doi:10.1242/jeb.030932.
- [14] Lauder GV, Lim J, Shelton R, Witt C, Anderson E, Tangorra JL. Robotic models for studying undulatory locomotion in fishes. *Mar Technol Soc J* 2011;45:41–55. doi:10.4031/MTSJ.45.4.8.
- [15] Rosic M-LN, Thornycroft PJM, Feilich KL, Lucas KN, Lauder GV. Performance variation due to stiffness in a tuna-inspired flexible foil model. *Bioinspir Biomim* 2017;12:16011. doi:10.1088/1748-3190/aa5113.

- [16] Jayne BC, Lauder GV. Speed effects on midline kinematics during steady undulatory swimming of largemouth bass, *Micropterus salmoides*. *J Exp Biol* 1995;198:585–602.
- [17] Drucker EG, Lauder GV. A hydrodynamic analysis of fish swimming speed: wake structure and locomotor force in slow and fast labriform swimmers. *J Exp Biol* 2000;203:2379–93.
- [18] Domenici P. The scaling of locomotor performance in predator-prey encounters: from fish to killer whales. *Comp Biochem Physiol - A Mol Integr Physiol* 2001;131:169–82. doi:10.1016/S1095-6433(01)00465-2.
- [19] Lauder GV, Drucker EG. Forces, fishes, and fluids: hydrodynamic mechanisms of aquatic locomotion. *News Physiol Sci* 2002;17:235–40. doi:10.1152/nips.01398.2002.
- [20] Dabiri JO. On the estimation of swimming and flying forces from wake measurements. *J Exp Biol* 2005;208:3519–32. doi:10.1242/jeb.01813.
- [21] Webb PW, Weihs D. Stability versus maneuvering: challenges for stability during swimming by fishes. *Integr Comp Biol* 2015;55:753–64. doi:10.1093/icb/icv053.
- [22] Noca F, Shiels D, Jeon D. Measuring instantaneous fluid dynamic forces on bodies, using only velocity fields and their derivatives. *J Fluid Struct* 1997;11:345–50. doi:10.1006/jfls.1997.0081.
- [23] van Oudheusden BW, Scarano F, Roosenboom EWM, Casimiri EWF, Souverein LJ. Evaluation of integral forces and pressure fields from planar velocimetry data for incompressible and compressible flows. *Exp Fluids* 2007;43:153–62. doi:10.1007/s00348-007-0261-y.
- [24] Yates GT. Hydromechanics of body and caudal fin propulsion. In: Webb PW, Weihs D, editors. *Fish Biomech.*, New York: Praeger Publishers; 1983, p. 177–213.
- [25] Vogel S. *Life in Moving Fluids: the Physical Biology of Flow*. 2nd ed. Princeton: Princeton University Press; 1994.
- [26] Pritchard PJ. *Fox and McDonald's Introduction to Fluid Mechanics*. 8th ed. Hoboken, NJ: John Wiley & Sons, Inc.; 2011.
- [27] Bale R, Shirgaonkar AA, Neveln ID, Bhalla APS, MacIver MA, Patankar NA. Separability of drag and thrust in undulatory animals and machines. *Sci Rep* 2014;4:1–11. doi:10.1038/srep07329.
- [28] Dubois AB, Cavagna GA, Fox RS. Pressure distribution on the body surface of swimming fish. *J Exp Biol* 1974;60:581–91.
- [29] Usherwood JR, Hedrick TL, McGowan CP, Biewener AA. Dynamic pressure maps for wings and tails of pigeons in slow, flapping flight, and their energetic implications. *J Exp Biol* 2005;208:355–69. doi:10.1242/jeb.01359.
- [30] Liu X, Katz J. Instantaneous pressure and material acceleration measurements using a four-exposure PIV system. *Exp Fluids* 2006;41:227–40. doi:10.1007/s00348-006-0152-7.
- [31] Akanyeti O, Chambers LD, Ježov J, Brown J, Venturelli R, Kruusmaa M, et al. Self-

- motion effects on hydrodynamic pressure sensing: part I. Forward–backward motion. *Bioinspir Biomim* 2013;8:26001. doi:10.1088/1748-3182/8/2/026001.
- [32] van Oudheusden BW. PIV-based pressure measurement. *Meas Sci Technol* 2013;24:32001. doi:10.1088/0957-0233/24/3/032001.
- [33] Dabiri JO, Bose S, Gemmell BJ, Colin SP, Costello JH. An algorithm to estimate unsteady and quasi-steady pressure fields from velocity field measurements. *J Exp Biol* 2014;217:331–6. doi:10.1242/jeb.092767.
- [34] de Kat R, van Oudheusden BW. Instantaneous planar pressure determination from PIV in turbulent flow. *Exp Fluids* 2012;52:1089–106. doi:10.1007/s00348-011-1237-5.
- [35] Laskari A, de Kat R, Ganapathisubramani B. Full-field pressure from snapshot and time-resolved volumetric PIV. *Exp Fluids* 2016;57:44. doi:10.1007/s00348-016-2129-5.
- [36] Drucker EG, Lauder G V. Locomotor forces on a swimming fish: three-dimensional vortex wake dynamics quantified using digital particle image velocimetry. *J Exp Biol* 1999;202:2393–412.
- [37] Müller UK, Van den Heuvel BLE, Stamhuis EJ, Videler JJ. Fish footprints: morphology and energetics of the wake behind a continuously swimming mullet (*Chelon labrosus* Risso). *J Exp Biol* 1997;200:2893–906.
- [38] Müller UK, Smit J, Stamhuis EJ, Videler JJ. How the body contributes to the wake in undulatory fish swimming: flow fields of a swimming eel (*Anguilla anguilla*). *J Exp Biol* 2001;204:2751–62.
- [39] Willert CE, Gharib M. Digital particle image velocimetry. *Exp Fluids* 1991;10:181–93. doi:10.1007/BF00190388.
- [40] Stamhuis EJ, Videler JJ. Quantitative flow analysis around aquatic animals using laser sheet particle image velocimetry. *J Exp Biol* 1995;294:283–94.
- [41] Feilich KL, Lauder GV. Passive mechanical models of fish caudal fins: effects of shape and stiffness on self-propulsion. *Bioinspir Biomim* 2015;10:36002. doi:10.1088/1748-3190/10/3/036002.
- [42] Alben S, Witt C, Baker TV, Anderson E, Lauder GV. Dynamics of freely swimming flexible foils. *Phys Fluids* 2012;24:51901. doi:10.1063/1.4709477.
- [43] Shelton RM, Thornycroft PJM, Lauder GV. Undulatory locomotion of flexible foils as biomimetic models for understanding fish propulsion. *J Exp Biol* 2014;217:2110–20. doi:10.1242/jeb.098046.
- [44] Quinn DB, Lauder GV, Smits AJ. Scaling the propulsive performance of heaving flexible panels. *J Fluid Mech* 2014;738:250–67. doi:10.1017/jfm.2013.597.
- [45] Quinn DB, Lauder GV, Smits AJ. Maximizing the efficiency of a flexible propulsor using experimental optimization. *J Fluid Mech* 2015;767:430–48. doi:10.1017/jfm.2015.35.
- [46] Donley JM, Dickson KA. Swimming kinematics of juvenile kawakawa tuna (*Euthynnus affinis*) and chub mackerel (*Scomber japonicus*). *J Exp Biol* 2000;203:3103–16.

- [47] Tytell ED. The hydrodynamics of eel swimming II. Effect of swimming speed. *J Exp Biol* 2004;207:3265–79. doi:10.1242/jeb.01139.
- [48] Winter D. *Biomechanics and motor control of human movement*. 4th ed. Hoboken, NJ: John Wiley & Sons, Inc.; 2009.
- [49] White FM. *Viscous Fluid Flow*. 3rd ed. Boston: McGraw-Hill Education; 2005.
- [50] Wang Z, Gao Q, Wang C, Wei R, Wang J. An irrotation correction on pressure gradient and orthogonal-path integration for PIV-based pressure reconstruction. *Exp Fluids* 2016;57:1–16. doi:10.1007/s00348-016-2189-6.
- [51] Gemmell BJ, Colin SP, Costello JH, Dabiri JO. Suction-based propulsion as a basis for efficient animal swimming. *Nat Commun* 2015;6:8790. doi:10.1038/ncomms9790.
- [52] Schlueter-Kuck K, Dabiri JO. Pressure evolution in the shear layer of forming vortex rings. *Phys Rev Fluids* 2016;1:12501. doi:10.1103/PhysRevFluids.1.012501.
- [53] Zar JH. *Biostatistical Analysis*. New Jersey, USA: Prentice Hall; 2010.
- [54] de Kat R, van Oudheusden BW. Instantaneous planar pressure determination from PIV in turbulent flow. *Exp Fluids* 2012;52:1089–106. doi:10.1007/s00348-011-1237-5.
- [55] Akanyeti O, Thornycroft PJM, Lauder GV, Yanagitsuru YR, Peterson AN, Liao JC. Fish optimize sensing and respiration during undulatory swimming. *Nat Commun* 2016;7:11044. doi:10.1038/ncomms11044.

Table 1. Rectangular foil – quantitative comparisons^a of forces and torques from three-dimensional tests.

Motion type	Laser position	Correlation Coefficient ^b (95% CI low, high)			RMSE%			Phase Lag % ^c		
		F_x	F_y	T_z	F_x	F_y	T_z	F_x	F_y	T_z
0angle	Midline ^d	0.963 (0.951, 0.972)	0.937 (0.917, 0.952)	0.9924 (0.9899, 0.9942)	30.3	12.7	7.3	0	1.5	0
	2 cm	0.985 (0.980, 0.989)	0.982 (0.976, 0.986)	0.9972 (0.9963, 0.9979)	15.9	12.2	10.1	0	3	0
	Edge	0.935 (0.915, 0.950)	0.989 (0.985, 0.991)	0.984 (0.978, 0.988)	30.3	30.5	25.4	-1.5	0	-1.5
heave	Midline	0.341 (0.212, 0.459)	0.976 (0.969, 0.982)	0.987 (0.983, 0.990)	45.8	8.2	7.7	9	-1.5	0
	2 cm	0.523 (0.414, 0.617)	0.968 (0.958, 0.976)	0.978 (0.971, 0.983)	51.3	13.4	12.1	-48	-3.0	-1.5
	Edge	0.355 (0.227, 0.471)	0.765 (0.701, 0.818)	0.942 (0.924, 0.956)	55.4	45.2	14.3	-57	-10.5	-1.5

0angle = 0° angle of attack motions; heave = heaving motions; 95% CI = confidence interval; RMSE% = root-mean-square error percentage.

^a Note that some quantitative analyses performed poorly at low force magnitudes and may therefore underestimate the agreement between the measured and calculated force and torque values. See Results section in the main text for details.

^b Normalized values.

^c Phase lags, as percentages of motion cycle periods, were determined by cross-correlation.

^d Due to unusual oscillations resulting from a loose screw, midline data were replaced with equivalent data from dynamic testing.

Table 2. Tail-shaped foil – quantitative comparisons^a of forces and torques from three-dimensional tests.

Motion type	Laser position	Correlation Coefficient ^b (95% CI low, high)			RMSE%			Phase Lag % ^c		
		F_x	F_y	T_z	F_x	F_y	T_z	F_x	F_y	T_z
0angle	Midline	0.949 (0.933, 0.961)	0.924 (0.900, 0.942)	0.970 (0.961, 0.977)	50.2	21.8	24.1	0	3	1.5
	Gap	0.887 (0.853, 0.913)	0.963 (0.951, 0.972)	0.969 (0.959, 0.976)	43.9	33.6	20.6	-3	-1.5	-3
heave	Midline	0.424 (0.303, 0.532)	0.924 (0.900, 0.942)	0.932 (0.911, 0.948)	43.0	22.7	12.5	-7.5	-4.5	3
	Gap	0.723 (0.649, 0.783)	0.983 (0.977, 0.987)	0.940 (0.922, 0.955)	36.8	11.9	22.8	0	-1.5	0

0angle = 0° angle of attack motions; heave = heaving motions; 95% CI = confidence interval; RMSE% = root-mean-square error percentage.

^a Note that some quantitative analyses performed poorly at low force magnitudes and may therefore underestimate the agreement between the measured and calculated force and torque values. See Results section in the main text for details.

^b Normalized values.

^c Phase lags, as percentages of motion cycle periods, were determined by cross-correlation.

Table 3. Dynamic tests – quantitative comparison^a of forces and torques at increasing actuation frequencies.

Motion type	Freq [Hz]	Correlation Coefficient ^b (95% CI low, high)			RMSE%			Phase Lag % ^c		
		F_x	F_y	T_z	F_x	F_y	T_z	F_x	F_y	T_z
0angle	0.5	0.248 (0.171, 0.322)	0.908 (0.893, 0.921)	0.914 (0.900, 0.926)	165.5	24.3	10.9	50	0.5	-1.0
	1.0	0.870 (0.840, 0.895)	0.992 (0.990, 0.994)	0.9914 (0.9893, 0.9932)	53.6	13.2	8.0	0	0	0
	1.5	0.963 (0.951, 0.972)	0.972 (0.962, 0.978)	0.9924 (0.9899, 0.9942)	30.3	12.7	7.3	0	1.5	0
	2.0	0.948 (0.929, 0.962)	0.971 (0.960, 0.979)	0.9947 (0.9926, 0.9961)	16.8	10.4	5.9	0	0	0
	2.5	0.929 (0.889, 0.950)	0.792 (0.713, 0.851)	0.9942 (0.9916, 0.9960)	14.7	19.5	6.4	0	0	0
heave	0.5	0.513 (0.451, 0.569)	0.869 (0.848, 0.888)	0.649 (0.601, 0.693)	279.2	28.9	21.7	1.5	0	-1.5
	1.0	0.605 (0.528, 0.672)	0.981 (0.976, 0.985)	0.956 (0.945, 0.965)	165.6	12.4	10.7	2.0	0	-1.0
	1.5	0.152 (0.013, 0.286)	0.883 (0.848, 0.910)	0.956 (0.942, 0.966)	82.0	15.9	8.3	10.5	-6.0	-1.5
	2.0	0.063 (-0.099, 0.222)	0.891 (0.852, 0.920)	0.958 (0.942, 0.969)	57.0	17.5	9.8	-86	-6.0	-2.0
	2.5	0.556 (0.417, 0.669)	0.988 (0.983, 0.992)	0.856 (0.799, 0.898)	36.8	18.3	15.9	2.5	0	-5.0

0angle = 0° angle of attack motions; heave = heaving motions; Freq = frequency; 95% CI = confidence interval; RMSE% = root-mean-square error percentage.

^a Note that some quantitative analyses performed poorly at low force magnitudes and may therefore underestimate the agreement between the measured and calculated force and torque values. See Results section in the main text for details.

^b Normalized values.

^c Phase lags, as percentages of motion cycle periods, were determined by cross-correlation.

Table 4. Static tests – quantitative comparison of forces and torques at increasing oncoming flow speeds.

Flow speed [cm/s]	Correlation Coefficient ^a (95%CI low, high)			RMSE%		
	<i>F_x</i>	<i>F_y</i>	<i>T_z</i>	<i>F_x</i>	<i>F_y</i>	<i>T_z</i>
10	-0.117 (-0.227, -0.003)	-0.132 (-0.242, -0.018)	-0.016 (-0.129, 0.098)	44.6	34.6	29.9
30	0.080 (-0.034, 0.192)	0.127 (0.014, 0.237)	0.170 (0.057, 0.278)	82.8	19.7	19.6
50	0.001 (-0.112, 0.115)	0.588 (0.508, 0.658)	0.278 (0.170, 0.379)	98.0	27.1	19.5

95% CI = confidence interval; RMSE% = root-mean-square error percentage.

^aNormalized values.

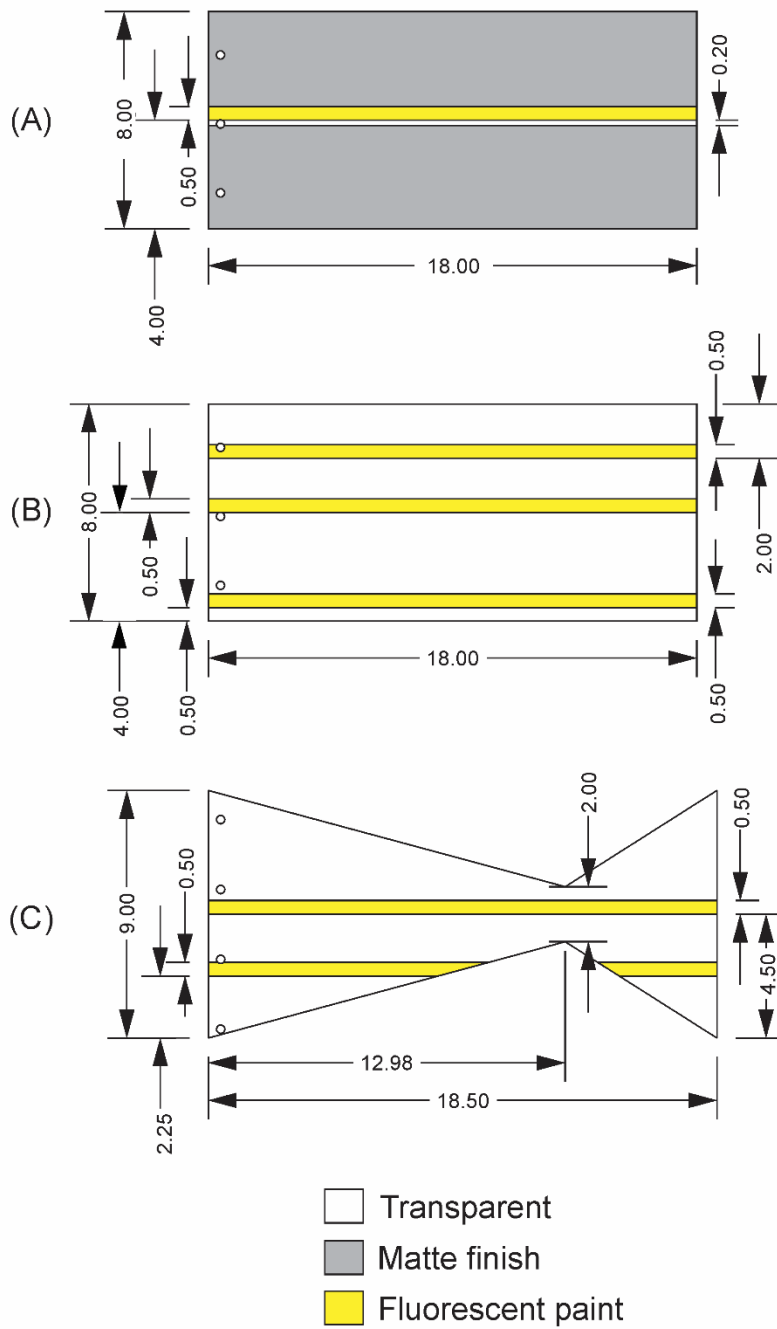


Fig. 1. Schematics of experimental foils.

(A) Rectangular foil. (B) Rectangular foil for 3D testing. (C) Tail-shaped foil. All dimensions are given in centimeters.

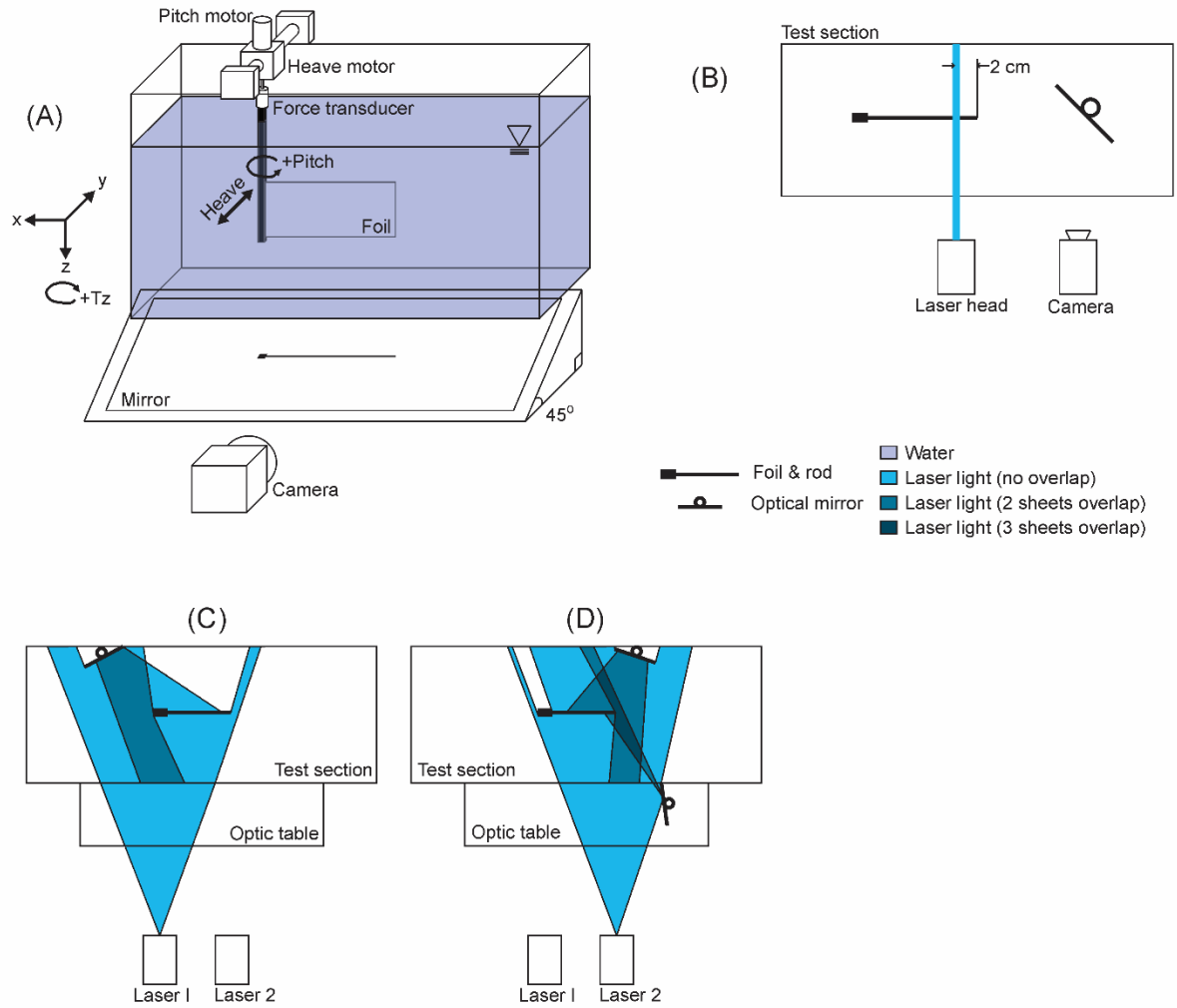


Fig. 2. Schematics of testing systems.

(A) Mechanical flapping foil testing apparatus in isometric view. (B) Overhead view of the transverse imaging setup. (C) Overhead view of the light sheet path of Laser 1. (D) Overhead view of the light sheet path of Laser 2. Laser 1 and Laser 2 were used simultaneously.

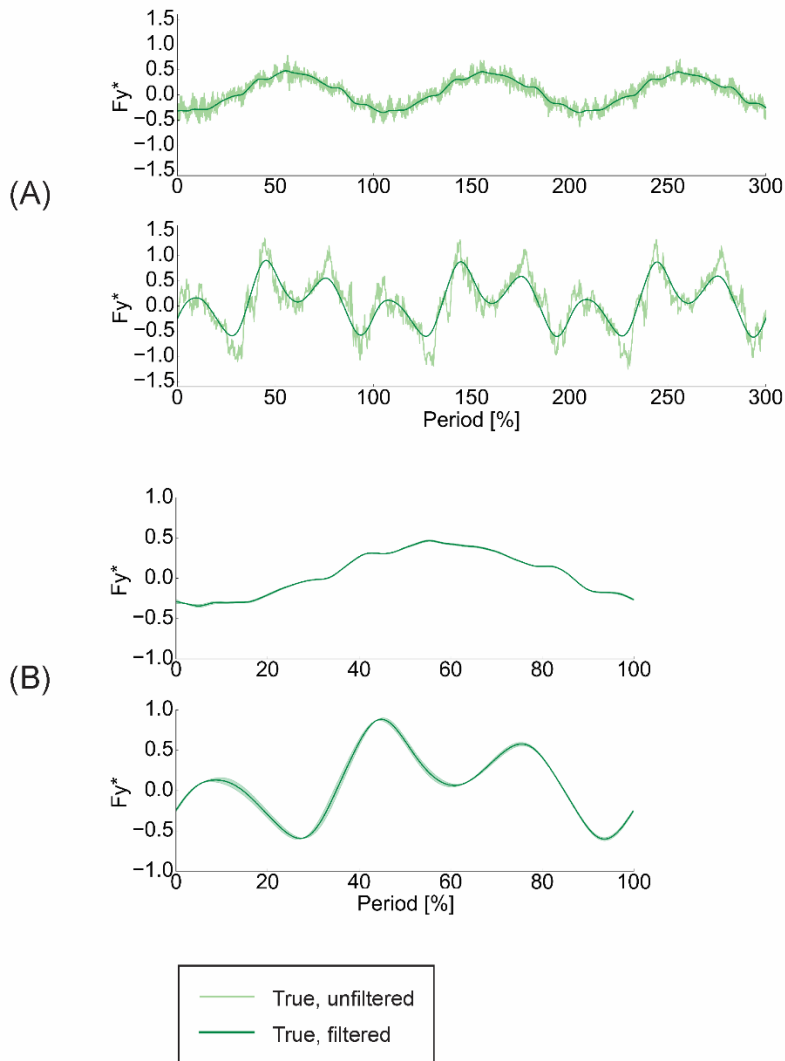


Fig. 3. Processing of highly repeatable measured force and torque data.

Measured force data were highly repeatable. (A) Example raw and filtered lateral force (F_y) traces, taken during dynamic testing. Three motion cycles during 1.0 Hz (top) and 2.0 Hz (bottom) 0° angle of attack motions are shown. (B) Filtered, phase-averaged traces of the data from (A). Silhouettes represent standard deviations. Streamwise forces (F_x) and vertical torques (T_z) followed similar trends to those displayed here.

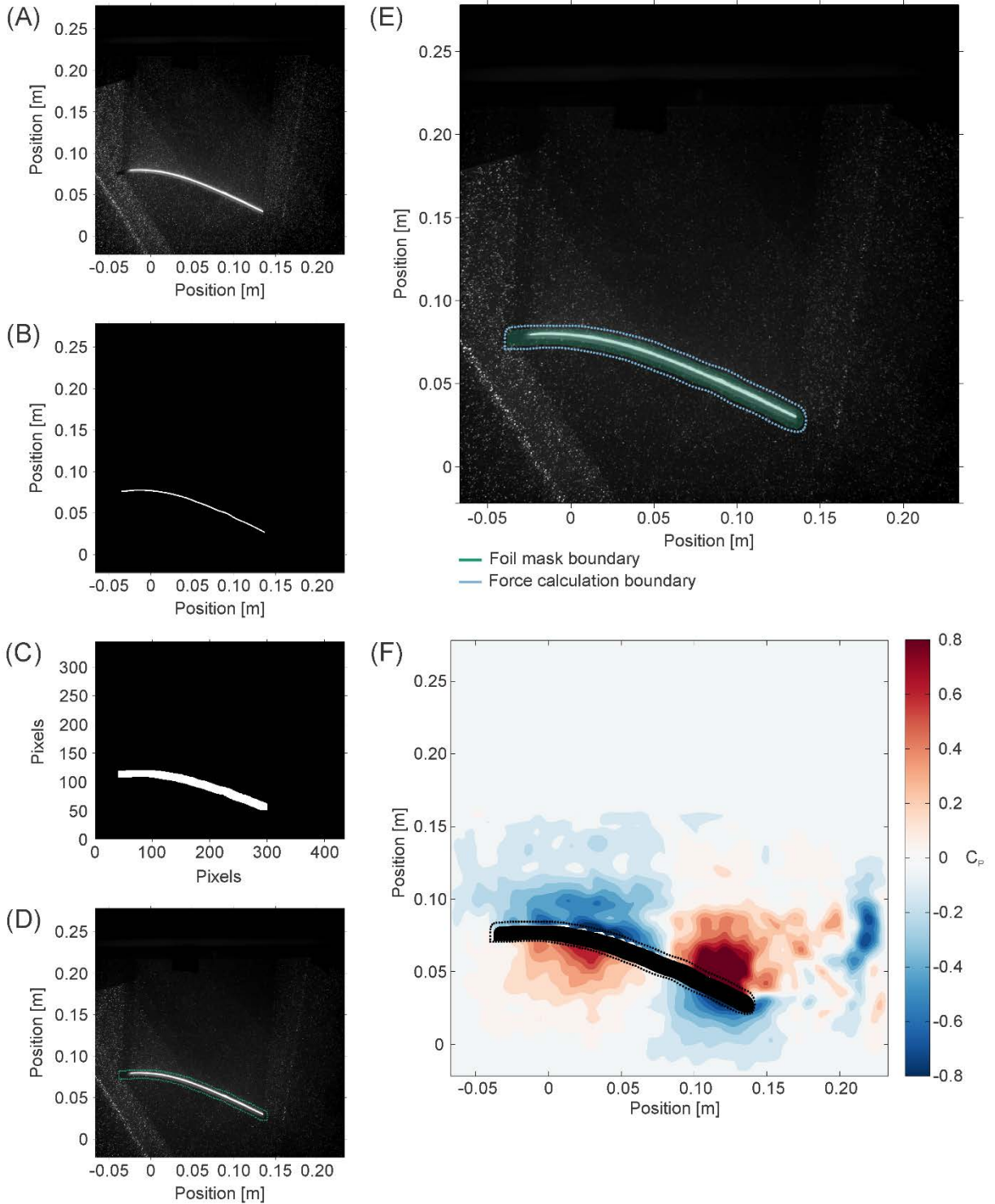


Fig. 4. Image processing steps in making foil masks and force calculation boundaries.

Boundary coordinates for foil masks and force calculation were generated using binary image processing. (A)-(D) illustrate mask generation, and the same process was used to produce force calculation boundaries. (A) A frame extracted from video of foil motion. Fluorescent paint at

the foil's midline appears as a bright line, and the portion of the foil below the light sheet is visible due to parallax of 3D structures. (B) The automatically-detected midline of the foil. (C) Binary image dilation widened the detected midline. (D) 200 equally-spaced points on the black-white boundary in (C) were extracted to use as a mask enclosing both the foil's midline and the portion of the foil visible below the light sheet. The points depicted here were smoothed to remove jagged edges. (E) Smoothed foil mask plotted as a silhouette, and the 200-point force calculation boundary produced by the same process. (F) Pressure contour for the video frame, with the foil mask and force calculation boundary drawn in black.

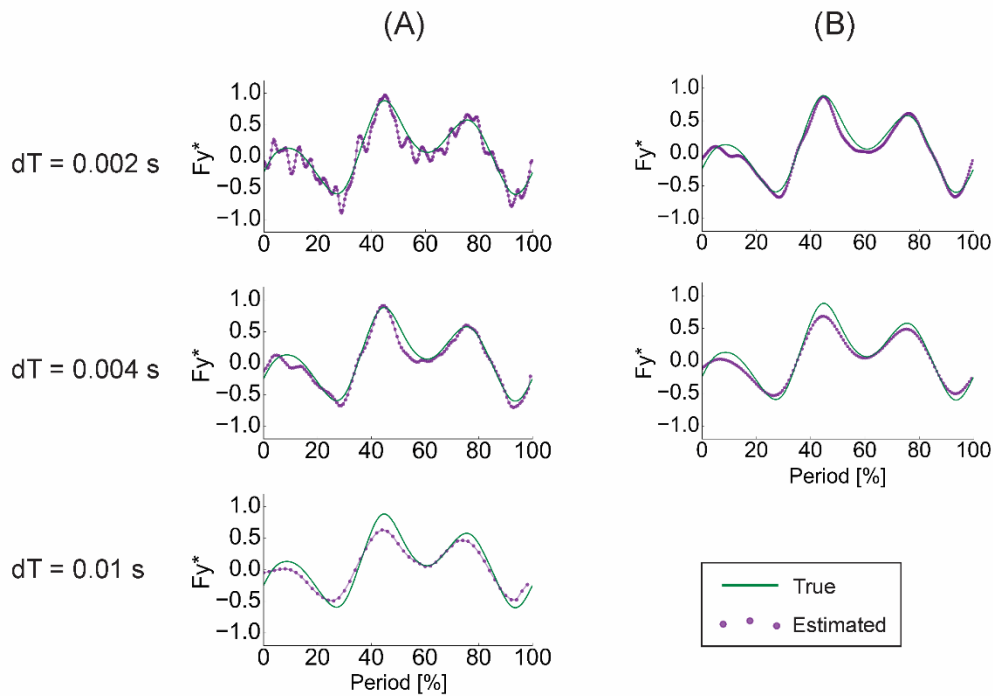


Fig. 5. Time step selection for pressure field calculation.

A comparison of the measured and calculated lateral force (F_y) values when the rectangular foil was operating in 0° angle of attack motions at 2.0 Hz actuation frequency under different time-steps. (A) The noise in the force trace from pressure-based force calculations decreased as time step (dT) increased. (B) When a low-pass filter was applied to the noisy time traces, nearly identical traces resulted, and these traces resembled the trace produced the time step was 0.01s. Streamwise forces (F_x) and vertical torques (T_z) followed similar trends to those displayed here.

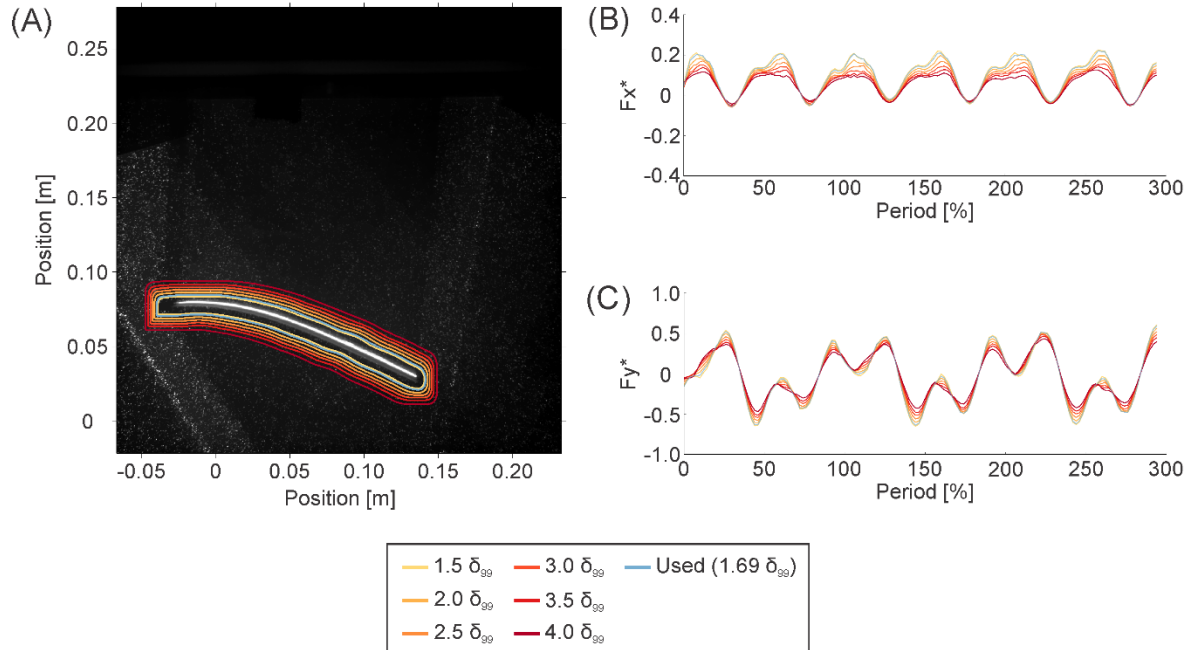


Fig. 6. Forces calculated at different boundary positions.

The magnitudes of the forces calculated using the pressure-based technique did not decline substantially when the calculation loop was within ~ 2.5 boundary-layer-widths (δ_{99}) from the foil's midline. To determine how close to the foil the force calculation loop needed to be for high accuracy results, the pressure-based calculation was conducted on multiple loops around the foil. Tests were conducted using pressure data from the dynamic, 2.0 Hz, 0° angle of attack trial. Loop position was measured in δ_{99} -widths from the foil's midline. (A) All of the calculation loops examined, drawn on the original image of the foil. (B) Non-dimensional streamwise forces (F_x^*) for the different loops, over three periods of foil motion. (C) Non-dimensional lateral forces (F_y^*) for the different loops, over three periods of foil motion.

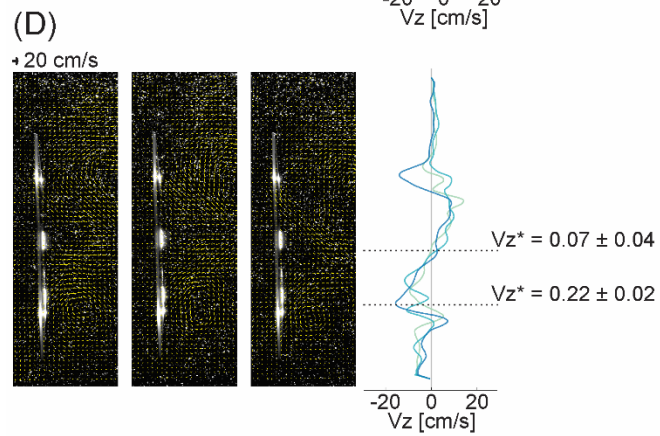
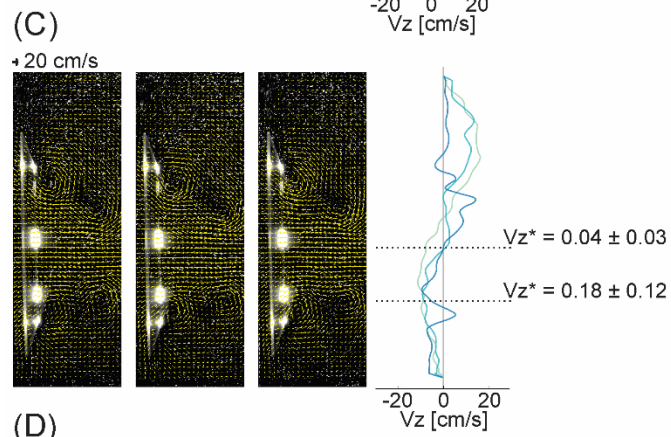
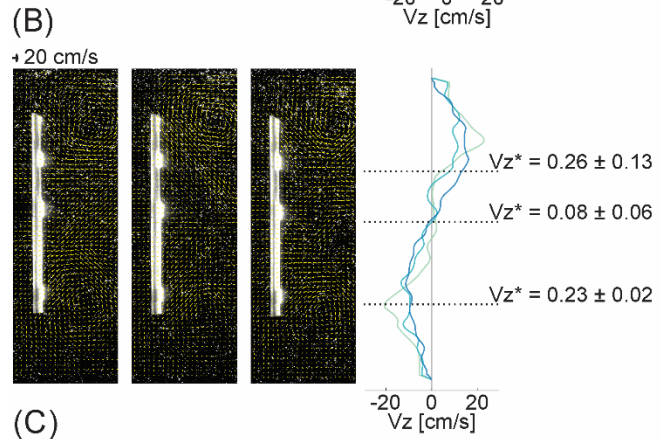
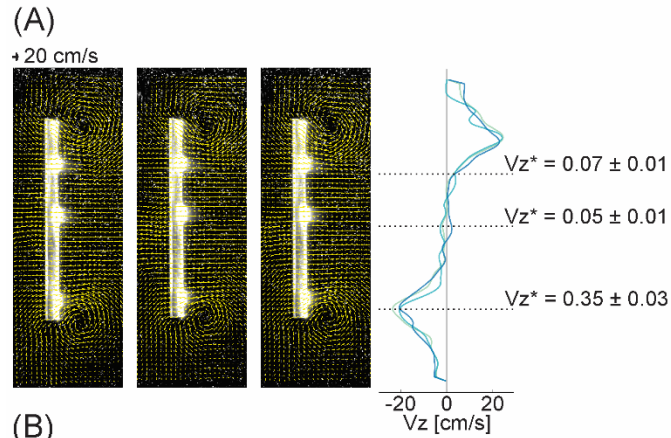


Fig. 7. Velocity vector fields in the transverse plane.

Velocity vector fields in the transverse plane as the foils approach direction reversal, for 1.5 Hz actuation frequency, 1.5 cm heave amplitude, and 30 cm/s oncoming flow (the conditions used for 3D testing). The foils move toward the left. Vertical velocities (V_z) were taken along a vertical line immediately to the right of the foil. Bright spots represent either the edges of the foil or the strips of fluorescent paint. Colors in velocity traces represent different trials. (A) Rectangular foil, 0° angle of attack program. (B) Rectangular foil, heaving program. (C) Tail-shaped foil, 0° angle of attack program. (D) Tail-shaped foil, heaving program. $V_z^* - V_z$ normalized by the total velocity at the measurement location, plus or minus standard deviation. Rect – rectangular foil. Tail – tail-shaped foil.

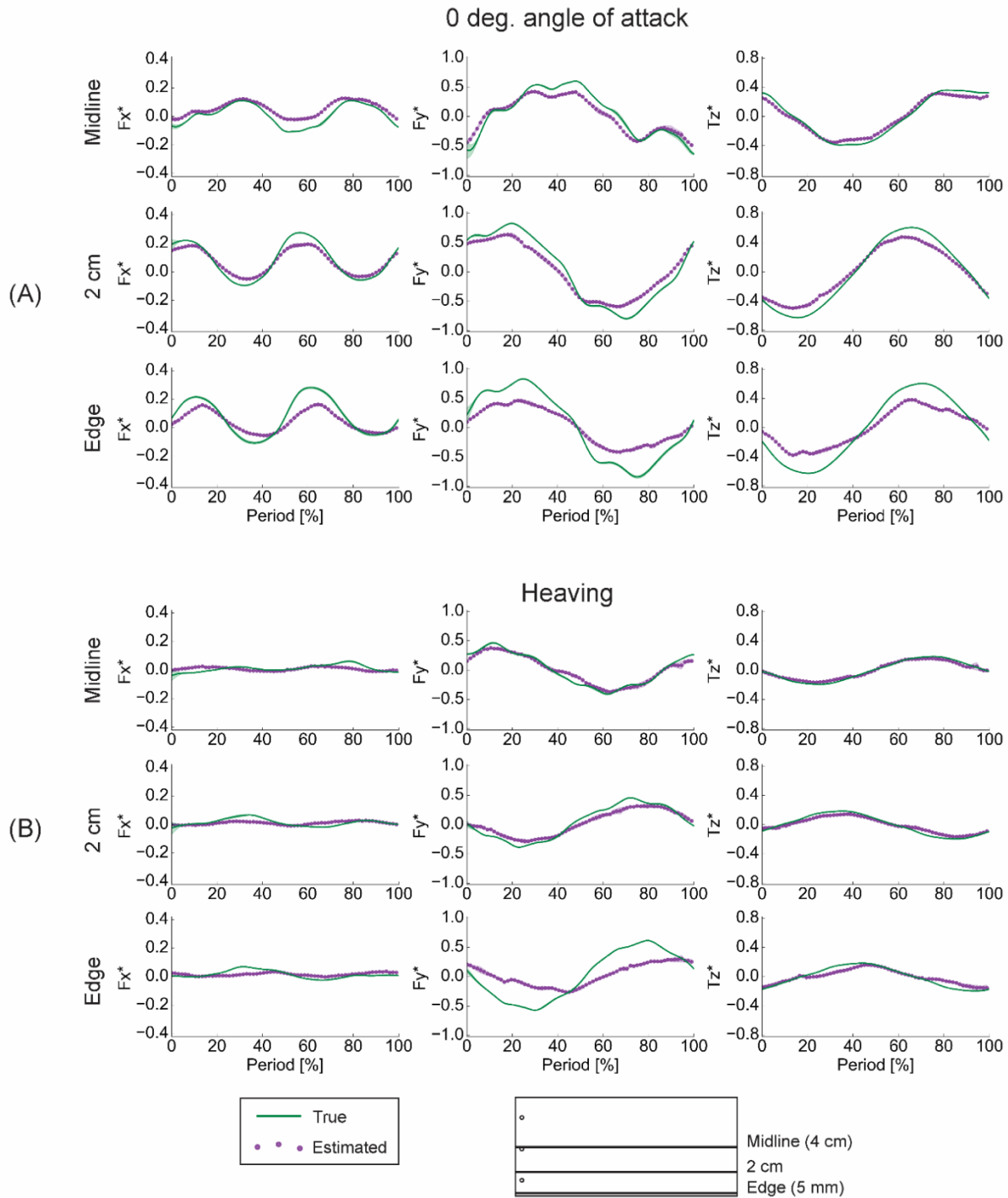


Fig. 8. Results of three-dimensional testing of the rectangular foil.

Comparisons of phase-averaged ($n=3$) measured and calculated force and torque time traces reveal that the pressure-based force calculation was generally able to accurately reproduce both the shape and magnitude of the measured trace, although the agreement declined with proximity to the foil's edge. (A) Results from 0° angle of attack motions. Due to unusual oscillations

resulting from a loose screw, midline data were replaced with equivalent data from dynamic testing. (B) Results from heaving motions. F_x – streamwise forces. F_y – lateral forces. T_z – torques about the vertical axis. Foil kinematics corresponded with the 1.5 Hz cases in dynamic testing (see Figs 10 and 11). Silhouettes represent standard deviations.

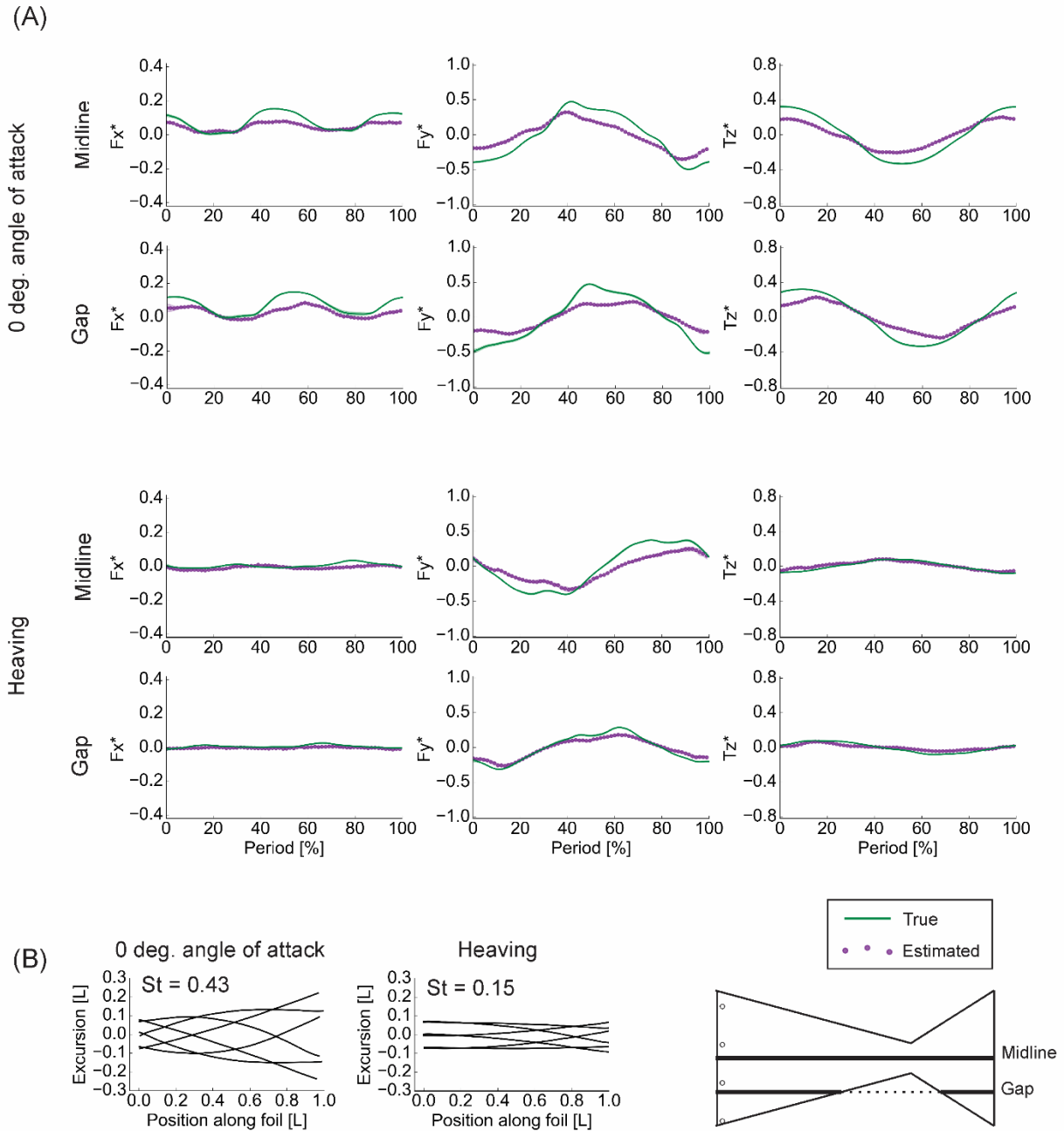


Fig. 9. Results of three-dimensional testing of the tail-shaped foil.

Despite the more complex shape of this foil, the pressure-based calculations were often able to accurately reproduce both the shape and the magnitude of the measured time traces. (A) Comparisons of phase-averaged ($n=3$) measured and calculated time traces. (B) Midline kinematics over one motion cycle. F_x – streamwise forces. F_y – lateral forces. T_z – torques about the vertical axis. St – Strouhal number. Silhouettes represent standard deviations.

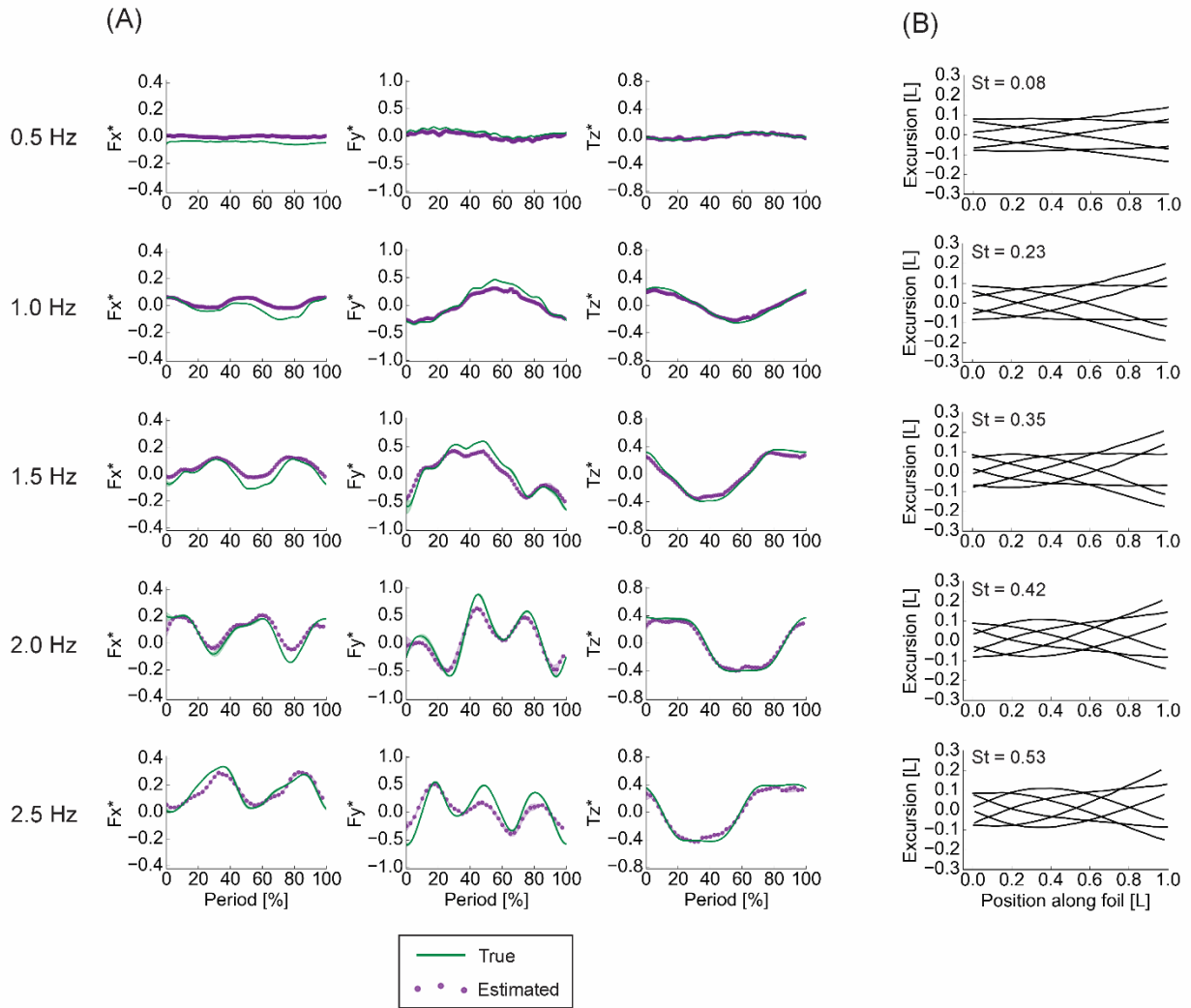


Fig. 10. Results of dynamic testing, 0° angle of attack motions, of the rectangular foil.

Generally, the pressure-based calculations were able to accurately reproduce both the shape and the magnitude of the measured time traces. Agreement declined slightly as actuation frequency increased. (A) Comparisons of phase-averaged ($n=3$) measured and calculated time traces. (B) Midline kinematics over one motion cycle, corresponding to the time traces on the left. F_x – streamwise forces. F_y – lateral forces. T_z – torques about the vertical axis. St – Strouhal number. Silhouettes represent standard deviations.

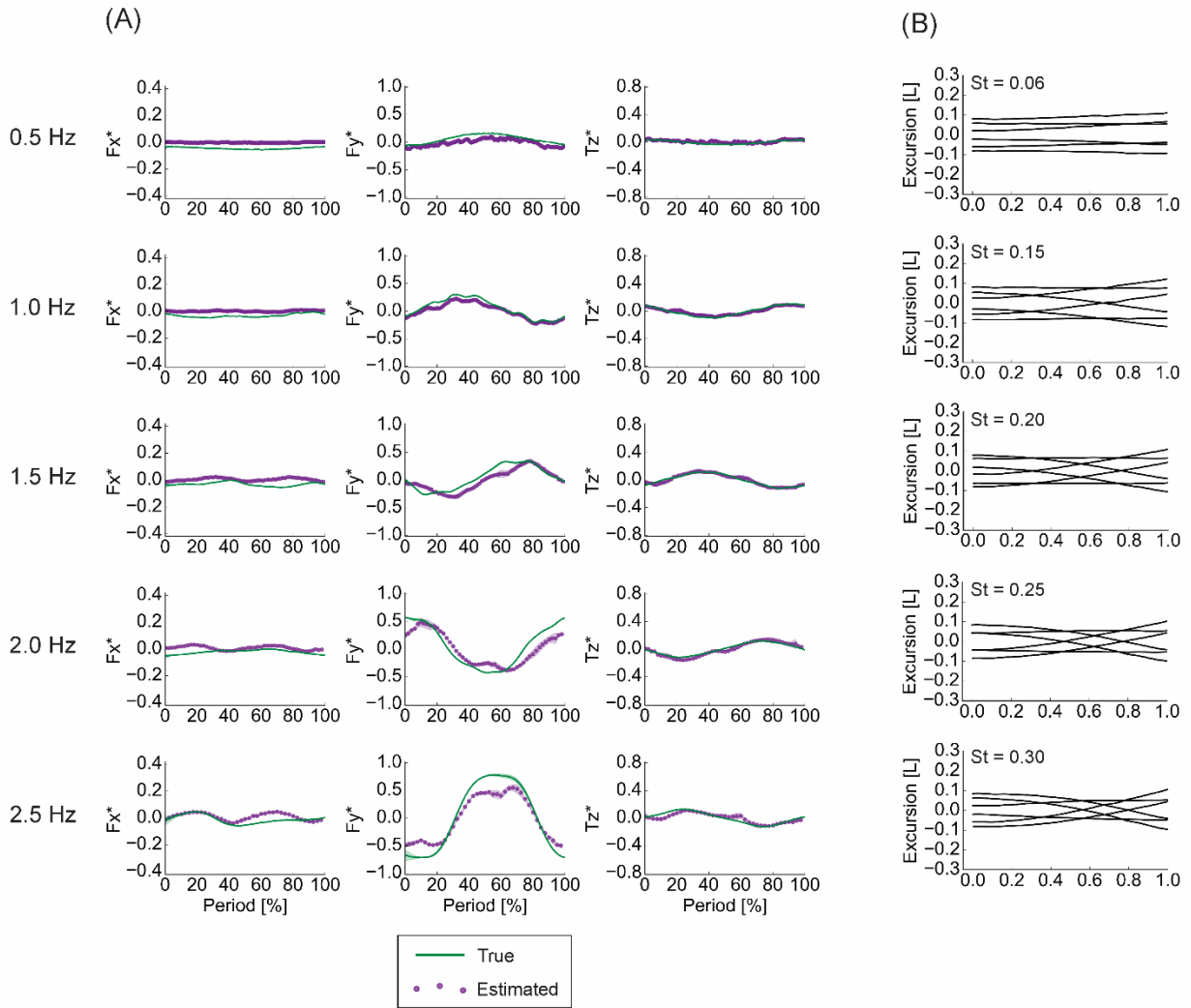


Fig. 11. Results of dynamic testing, heaving motions, of the rectangular foil.

Generally, the pressure-based calculations were able to accurately reproduce both the shape and the magnitude of the measured time traces, but less so than during 0° angle of attack motions. Agreement declined slightly as actuation frequency increased. (A) Comparisons of phase-averaged ($n=3$) measured and calculated time traces. (B) Midline kinematics over one motion cycle, corresponding to the time traces on the left. F_x – streamwise forces. F_y – lateral forces. T_z – torques about the vertical axis. St – Strouhal number. Silhouettes represent standard deviations.

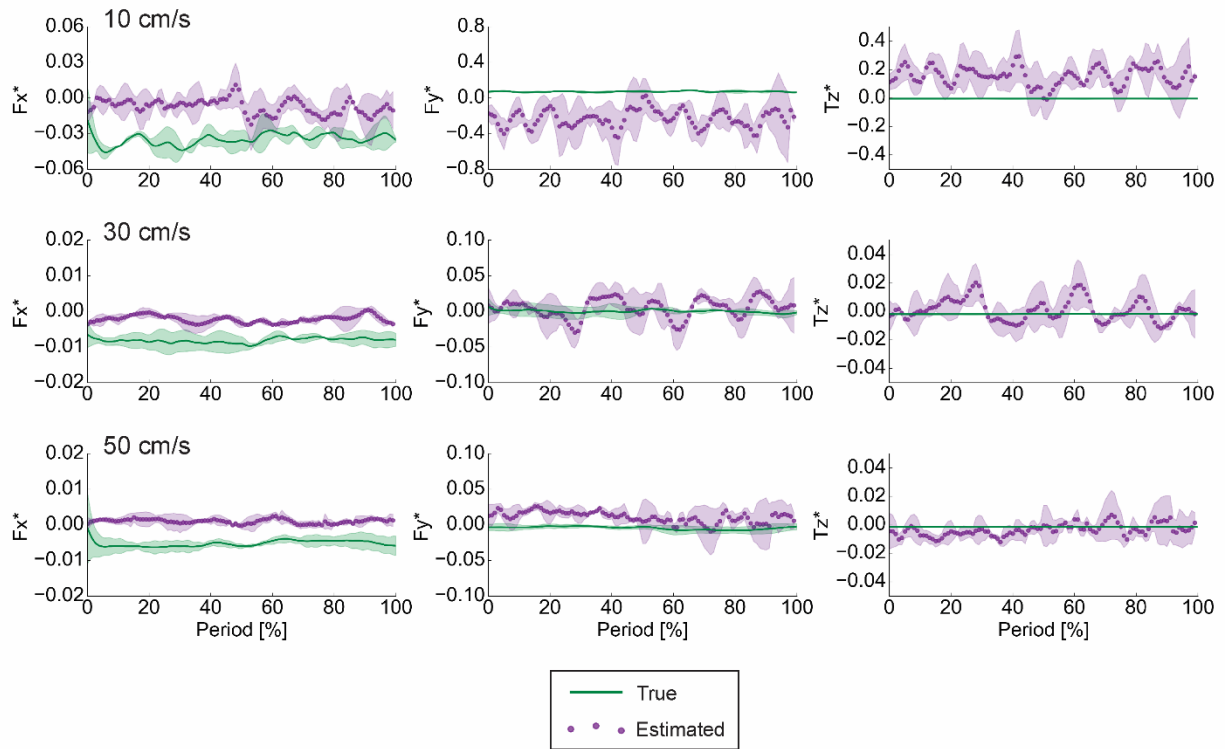


Fig. 12. Results of static testing of the rectangular foil.

In the static case, where shear forces dominate, the pressure-based calculations were not able to accurately predict locomotor forces and torques. For the comparisons of phase-averaged ($n=3$) measured and calculated time traces, note that the y-axis scales vary among oncoming flow speeds and differ from those in other figures. F_x – streamwise forces. F_y – lateral forces. T_z – torques about the vertical axis. Silhouettes represent standard deviations.

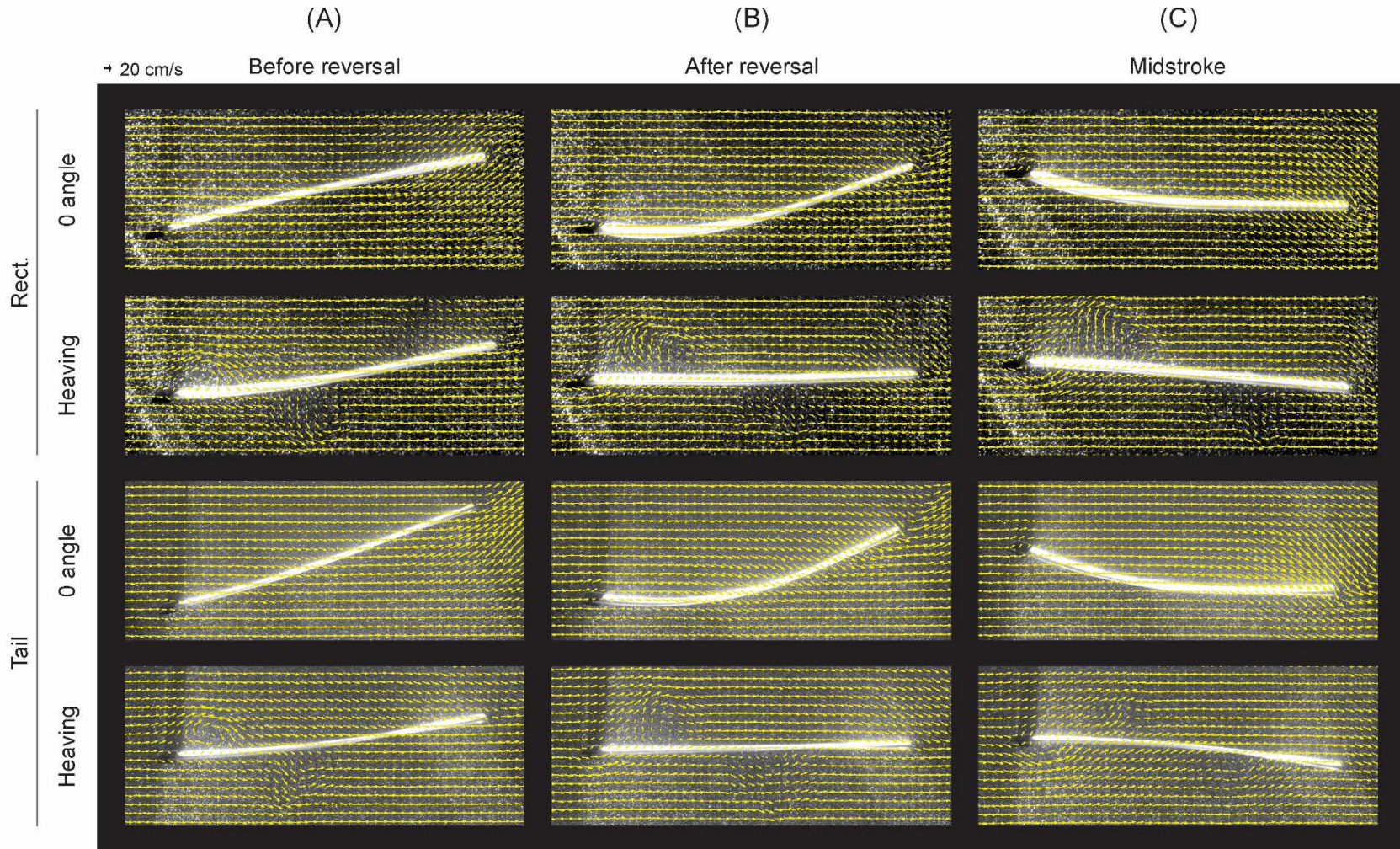


Fig. 13. Velocity vector fields in the horizontal plane, at the foil's midline.

Velocity vector fields at the foils' midlines revealing the differences in flow structures around the rectangular (Rect) and tail-shaped (Tail) foils during 0° angle of attack and pure heaving motions at three points in a stroke cycle. The foils were moved at 1.5 Hz

actuation frequency and 1.5 cm heave amplitude, in an oncoming flow of 30 cm/s. Before direction reversal, the foils move downward. While flow moves smoothly along the foils during 0° angle of attack motions, in the heaving program, a leading edge vortex is formed, shed, and destroyed in the succession of images.

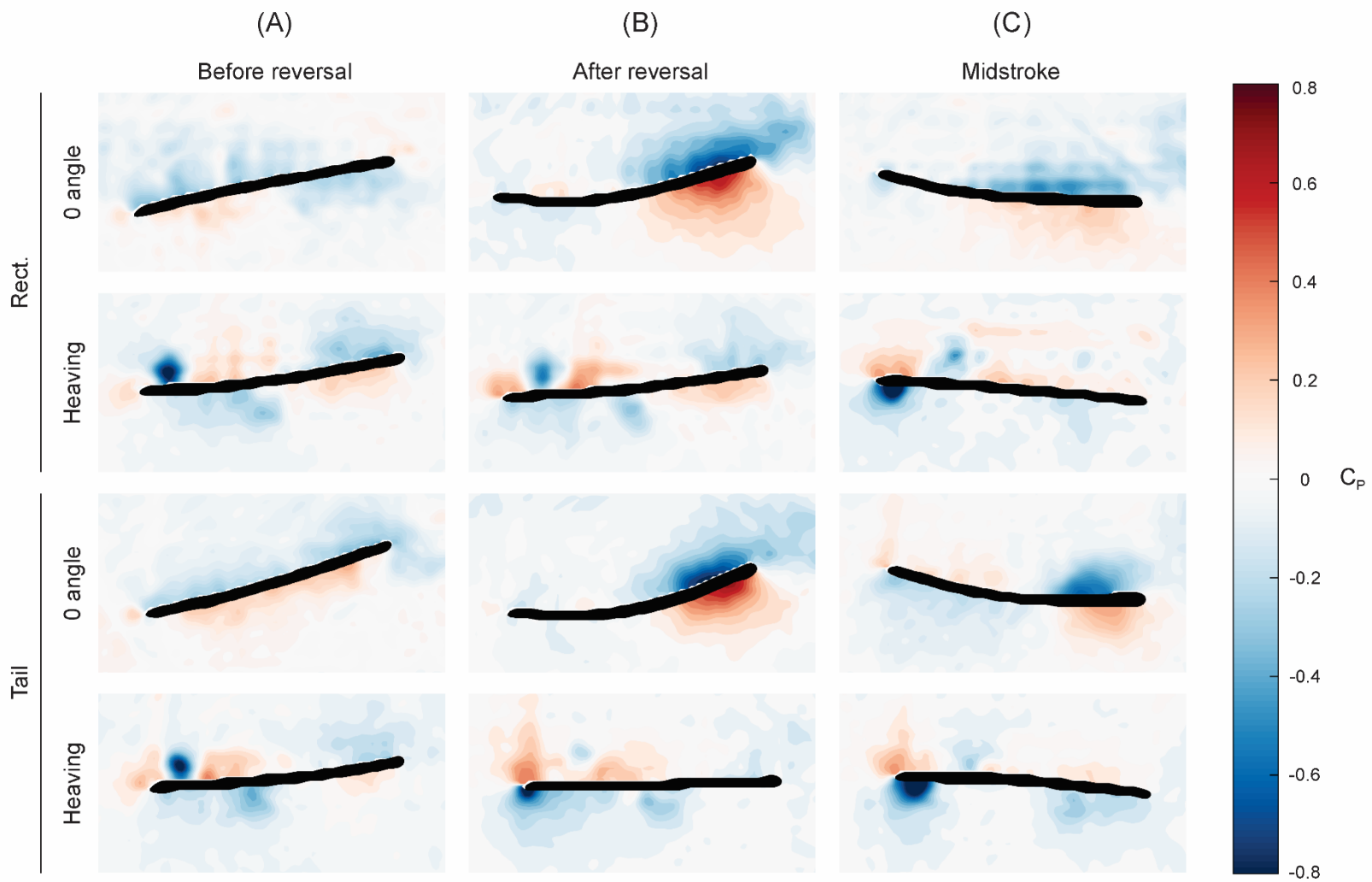


Fig. 14. Pressure fields in the horizontal plane, at the foil's midline.

Pressure fields at the foils' midlines around the rectangular (Rect) and tail-shaped (Tail) foils during 0° angle of attack and pure heaving motions at three points in a stroke cycle, corresponding to the snapshots in Fig 13. The foils were moved at 1.5 Hz actuation frequency and 1.5 cm heave amplitude, in an oncoming flow of 30 cm/s. Before direction reversal, the foils move downward. Color bar indicates the coefficient of pressure (C_p). During 0° angle of attack motions, pressure gradients peak near the trailing edge. In the heaving program, pressure peaks in the leading edge vortex, and deteriorates into complex patterns as the vortex is impacted by the foil.

.